CRYOMILLING OF ALUMINUM-BASED AND MAGNESIUM-BASED METAL POWDERS

by

Adam J. Maisano

Thesis submitted to the faculty of the
Virginia Polytechnic Institute and State University
in partial fulfillment of the requirements for the degree of

MASTER OF SCIENCE
in
Materials Science and Engineering

Approved by:

Dr. Stephen L. Kampe, Chairman
Dr. Alexander O. Aning
Dr. William T. Reynolds

January 13, 2006
Virginia Tech
Blacksburg, Virginia

Keywords: Cryomilling, Nanocrystalline materials, Al-Mg alloys, X-ray diffraction, Crystallite size, Hardness

Copyright 2006, Adam J. Maisano

Cryomilling of Aluminum-based and Magnesium-based Metal Powders

Adam J. Maisano

ABSTRACT

Ball milling has been shown to produce nanostructures in metal powders through severe repetitive deformation. Ball milling at cryogenic temperatures (cryomilling) is more effective in this capacity due to the low temperature by slowing recovery and minimizing diffusion distances between different components. Nanostructured metals are of interest because of their unique physical and mechanical properties. The result of cryomilling is powder consisting of crystallites on the order of 30 – 50 nm. In order to characterize the properties of this material, it is often necessary to consolidate the powder, which is often difficult without causing significant grain growth. In this work, aluminum-rich and magnesium-rich alloys of varying composition are produced by cryomilling and characterized by x-ray diffraction. A novel consolidation process called high shear powder consolidation (HSPC) is used to densify as-received and as-milled powders with minimal growth. The construction of a cryomill, along with a modification for improving process yield, has provided a platform for the study of nanocrystalline metals. It has been shown that bulk nanocrystalline materials are attainable and that alloy composition influences mechanical properties.

Acknowledgements

I would like to thank my advisors, Dr. Stephen Kampe and Dr. Alex Aning, for their guidance and support throughout my research. Your knowledge and suggestions have been invaluable. I am also grateful to Dr. William Reynolds for his advice and for serving on my committee.

To Dr. Jeff Schultz, thank you for your technical assistance and always being willing to talk. Your company on the bike has been enjoyable as well.

To the Kamposites Group, your suggestions were always appreciated as were friendships away from school. Best of luck to all of you. David Berry, thanks for keeping our department going.

I would also like to thank Dr. Andrew Payzant and Dr. Arvid Pasto in the High Temperature Materials Laboratory at the Oak Ridge National Laboratory for their time and assistance with the x-ray analysis portion of my project.

I would especially like to thank my parents for their support throughout my time at Virginia Tech. Your love, counseling, encouragement, and money have helped me to get this far. Jody, you are an inspiration. Aunt Josie and Uncle Deb, thank you for everything over the last 6.5 years.

And to Lisa, I can only say that your love and friendship make me better.

Table of Contents

List of Figures

List of Tables

1 Chapter One – Introduction

Nanocrystalline metals are of significant research interest due to their high strength. There exists many techniques for fabricating these materials, such as mechanical alloying (MA), rapid solidification, plasma processing, vapor deposition, high pressure torsion, equal channel angular processing [1]. Most of these methods, however, are only capable of producing small volumes for research purposes, not the large quantities needed for structural applications [2]. Of these techniques, MA has received much attention as a means to produce larger amounts of nanocrystalline powder.

Cryomilling, a form of MA that uses a liquid nitrogen bath, is particularly effective in this capacity due to its low temperature which slows recovery and minimizes diffusion distances between different components. It has also been shown to produce alloys with solute concentration beyond equilibrium at room temperature.

In this study, aluminum-rich and magnesium-rich alloys of varying composition will be produced by cryomilling. The main objectives of this thesis are to:

i. fabricate Al alloys containing 0, 4, 7, and 10 wt.% Mg by cryomilling
ii. fabricate Mg alloys containing 0, 4, 7, and 10 wt.% Al by cryomilling
iii. consolidate each material by high shear powder consolidation (HSPC)
iv. characterize the crystallite size and lattice strain of all powder and bulk materials by x-ray diffraction.

The remainder of the thesis is organized as follows:

Chapter Two reviews MA and MA at cryogenic temperatures, or cryomilling. The concepts of extended solubilities, strengthening mechanisms, and ductilization of

nanocrystalline materials are also introduced. Powder consolidation techniques such as hot isostatic pressing, extrusion, and HSPC are discussed, as well as the theories behind x-ray diffraction of crystalline materials.

Chapter Three describes the experimental procedure used in this project, including construction of the cryomill. The methods used for mechanical testing and determination of crystallite size and strain are presented. Chapter Four is a discussion of the results obtained in Chapter Three. Chapters Five and Six summarize the conclusions drawn from this study and the recommendations for future work.

2 Chapter Two – Background

The focus of this work is the fabrication and characterization of nanocrystalline metal powders. To address these topics, this chapter will be divided into four main sections. The first section will discuss the principles of MA. Mechanical alloying at cryogenic temperatures, or cryomilling, is the focus of the second section, including strengthening mechanisms at work in nanocrystalline materials, especially those pertinent to the aluminum-magnesium system. Some previous works on ductilization of nanocrystalline matrices are also discussed. High shear powder consolidation (HSPC) is addressed in the third section, while the fourth section discusses x-ray diffraction of crystalline materials, particularly its use in characterizing crystallite size and strain in the material.

2.1 Mechanical Alloying

Mechanical attrition by high-energy ball milling has been developed as a method to produce large quantities of nanostructured materials [3]. Ball milling produces these nanostructures by the structural decomposition of coarser-grained powder materials by severe repetitive fracture and deformation [3, 4]. Mechanical alloying (MA) has been established as a powerful tool to fabricate a wide range of metals, alloys, intermetallics, ceramics, and composites, including non-equilibrium materials (e.g. amorphous, quasicrystalline, nanocrystalline) [1, 3].

During MA, powder particles are repetitively cold welded and fractured due to the high-energy collision of the milling media. It is this deformation at high strain rates that

allows nanostructured materials to be produced [3]. Cold welding minimizes the diffusion distance between phases, and the fracture events lead to clean surfaces free of oxide layers, which also serve to facilitate diffusion [5]. Figure 1 shows a schematic of how powder particles are welded and fractured between the colliding media. The diagram on the left shows two components being impacted between the balls, while the one on the right shows the beginning stages of alloyed particles with their layered structures. This lamellar structure has been observed by Zhou et al. [6] and Park et al. [1].

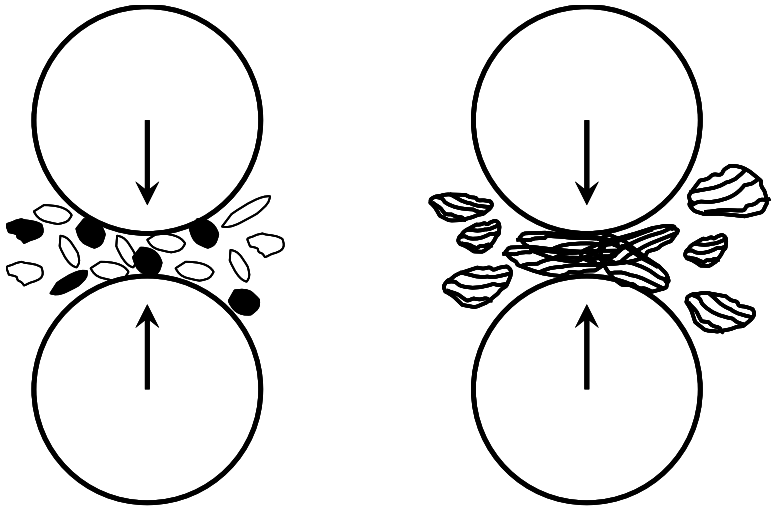

Figure 1: Diagrams of colliding milling media during mechanical alloying

When discussing the subject of crystalline metals, the terms *particle size*, *grain size*, and *crystallite size* are commonly used, often interchangeably in the literature. *Particle size* has the loosest definition of the three. It can be used to describe the size of powdered material (e.g. -325 mesh, or 44 μm), or to describe the diameter of the substructure (e.g. grains, crystals, or phases) in a metal, usually viewed using a microscope. *Grain size* is the most commonly used term, and is the conventional means of referring to the size of the crystals that comprise a metal's microstructure. These

crystals have well-defined, high-angle boundaries, and sometimes contain a substructure. The term *crystallite size* refers to the size of this substructure, which is characterized by low-angle boundaries. It is used when the size of the individual crystals is less than about 100 nm [7, 8]. Figure 2 compares the relative sizes of particles, grains, and crystallites. In a nanocrystalline material, it is not possible to have a substructure, so a "crystallite" is the smallest component [8]. Because the typical objective of MA is to achieve a nanostructured material, *crystallite size* is the common term used by those studying MA, and so will be used throughout this thesis to avoid confusion.

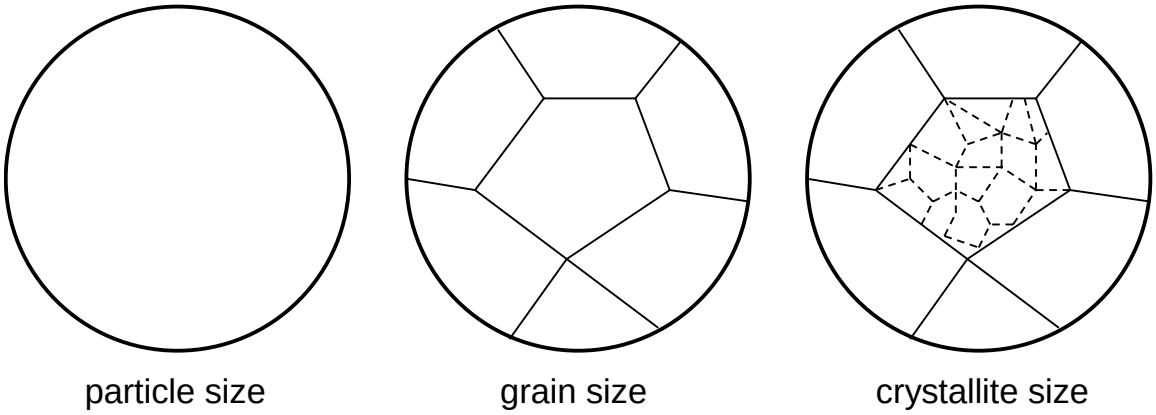

Figure 2: Relative comparison of particle size, grain size, and crystallite size

Thus far, MA has been discussed on a macro-scale in terms of welding and fracturing, but the mechanisms for crystallite size formation are more complex. This process involves three stages [3]:

i. The deformation is localized in shear bands consisting of a high density array of dislocations.

ii. At a certain strain level, these dislocations annihilate and rearrange to form small-angle grain boundaries separating the individual crystallites. During further attrition, the sample volume exhibiting small crystallites (20 – 30 nm) extends throughout the entire sample.

iii. The orientations of the crystallites become completely random with respect to their neighboring crystals, implying rotation.

Steady state deformation is observed when the dislocation generation rate is balanced by the annihilation rate [3].

Another event contributes to crystallite size refinement during MA. The motion of the crystallites within the shear band leads to impingement on neighboring crystallites and generates local inhomogeneous elastic strains [3]. To relieve these strains, nanovoids approximately 1 nm in diameter form, leading to the development of a crack, which eventually subdivides the crystallite [3].

2.1.1 Mechanical Alloying at Cryogenic Temperatures

It has been demonstrated that ball milling at cryogenic temperatures, or cryomilling, is capable of producing a nanostructure in various metals and alloys [1, 2, 6, 9-12]. Cryomilling differs from MA for two main reasons: the low temperatures are reached by mechanically alloying in a bath of liquid nitrogen, and a lower-energy milling level is used. Because of the cryogenic milling temperature, recovery in the material is less effective, which reduces the time to produce nano-sized crystallites [6, 13]. With the exception of this fact, cryomilling follows the same mechanisms and processes as MA at ambient temperatures discussed previously.

2.1.2 Extended Solubilities

Gubicza et al. reported on the effect of milling time on the concentration of Mg in solid solution. An Al-Mg powder mixture containing nominally 6 wt.% Mg milled at room temperature for 3 hours was found to have 5.52 wt.% Mg in solid solution [5]. The

equilibrium solubility limit of Mg in Al at 100 °C is 1.9 wt.%, and at room temperature, it is certainly below this value [5]. Thus, the equilibrium solubility limit is capable of being exceeded. The solid solubility of Mg in Al was reported to exceed 7.5 wt.% by Zhou et al. [14] and Zhang et al. [15] for cryomilled powders. The repetitive welding and fracturing of the powder particles physically alloy the materials beyond the equilibrium concentration. This is helped by the fact that, at the same time, the diffusion distance between the atoms of the different components is minimized [5].

2.1.3 Strengthening Mechanisms in Nanocrystalline Metals

The strengthening of metals is derived from limiting the mobility of dislocations through the lattice [16]. Three mechanisms are notably introduced to the strengthening effect in cryomilled materials: crystallite size strengthening, dispersion strengthening, and solid solution strengthening. These topics are addressed here but are discussed more fully later in this thesis.

Crystallite sizes can be significantly reduced by cryomilling and can be retained after subsequent consolidation. It has been demonstrated that decreasing the crystallite size of Al alloys from 500 nm to 50 nm results in a continuous increase in strength following the Hall-Petch equation [17]. Rodriguez et al. also observed strengthening due to crystallite size refinement in cryomilled Inconel™ 625 [12]. The Hall-Petch relationship describes the strengthening in metals as a function of crystallite diameter, d, according to

$$\sigma_{ys} = \sigma_o + k_y \cdot d^{-1/2} \tag{1}$$

where σ_{ys} is the yield or flow stress of the metallic alloy, σ_o is the reference stress (associated with the strength of a "large" grained polycrystal), and k_y the strengthening

constant which quantifies the material's sensitivity of strength to crystallite size. Dislocations encounter crystallite boundaries more quickly in materials with small crystallite size, thereby requiring higher applied stresses for continued deformation; i.e. applying stress and strengthening it. Although the Hall-Petch relationship was developed for materials with conventional crystallite sizes (greater than 0.1 μm), Sevillano et al. claim that the equation holds for nanocrystalline materials above a threshold of about 10 nm [18]. Others suggest that strength may fall below Hall-Petch predictions for crystallite sizes below 20 nm due to the absence of dislocation pile-up and modulus softening by the high volume fraction of boundary material [13].

Contamination is inevitable during cryomilling. Abrasions from the milling media or vessel are impurities in the powder sample [2]. Cryomilling also introduces nitrogen and oxygen into the powder, which form nitride and oxide dispersoids. These impurities and dispersoids act as strong obstacles to dislocation motion in cryomilled materials [2, 9, 10, 13, 17]. The Orowan equation describes dispersion strengthening as

$$\sigma_{ys} = \sigma_o + \frac{2.4 \cdot G \cdot b}{L_{e-e}} \tag{2}$$

where σ_o is the reference stress, G is the shear modulus of the matrix, b is the magnitude of the Burger's vector of the matrix, and $L_{e\text{-}e}$ is the edge-to-edge spacing between the dispersed particles [2, 17]. The factor 2.4 in Equation 2 is related to the Taylor factor, which provides a conversion from single-plane shear slip to polycrystalline normal stresses.

Solid solution strengthening is the effect seen when one element of a different atomic size becomes dissolved in another. The result is a strain field surrounding the interstitial or substitutional atom [16]. The strain field impedes dislocation motion,

consequently strengthening the material. This effect can be quantified by the Fleisher model for solid solution strengthening, which is discussed in detail in section 4.4.2.3.

2.1.4 Ductilization Using Aluminum Phases

The increased strength described above comes at the expense of ductility. This concept is fundamental in crystalline materials. Improvements to the ductility of nanostructured metals has been accomplished by incorporating larger crystallites into a fine crystallite matrix, giving a bimodal grain size distribution [2]. Added ductility would be a desirable for the engineering of structural components to avoid catastrophic failure. Witkin et al. [2] reported that cryomilled and consolidated Al-7.5 wt.% Mg had a yield strength more than four times that of Al 5083 (nominally 4.5 wt.% Mg), but a failure strain five times less. By adding 15 and 30 wt.% unmilled Al, the yield strength decreased from 641 MPa to 630 MPa and 554 MPa, but failure strain increased from 1.4% elongation to 2.4% and 5.4%, respectively [2]. Ductilization of nanocrystalline materials is attainable when approached with a compositing method.

2.1.5 Consolidation by Hot Isostatic Pressing and Extrusion

The end result of cryomilling is powder which is more difficult to characterize relative to bulk forms. The problem with most forms of consolidation is that they involve elevated temperatures. Hot isostatic pressing (HIP) and extrusion are common processes used [1, 2, 17]. Mohamed et al. and Witkin et al. noted that thermo-mechanical processes such as these cause the crystallite size to increase by more than a factor of five [13, 17]. Obviously, this is undesirable for studying a material in its “as-cryomilled” state.

One aspect that HIP/extrusion have in their favor is that the oxides, nitrides, and impurities from cryomilling play a critical role in retarding the growth of the crystallites, despite the fact that they alter the chemical composition [2, 10].

2.2 High Shear Powder Consolidation

High shear powder consolidation (HSPC) is a solid-state, friction-based powder metallurgy process developed by Metalmorf Technologies, LLC [19]. The HSPC has its foundations in friction-stir welding, but takes it a step farther to fabricate materials and structures. Friction-stir welding is a method used to mechanically join two parts. This joining can either be achieved by rotating one (or both) of the parts being joined to "weld" them by shearing forces and heat from friction, or by "stirring" the material along the interface of the parts.

HSPC was originally considered as a means to repair holes or to modify the local properties in metal plates; however, it is also capable of creating fully dense alloys and composites through high-shear processing [19]. The materials manufactured by HSPC are then able to be used for prototyping of structural components. In HSPC, a vertical milling machine with computer numerical control (CNC) is modified for the purposes of powder consolidation. A cylindrical stirring tool made of high-speed steel is used in place of the machining bit in the spindle. The powder to be consolidated is placed in a hole or on the substrate, and with the tool rotating at high RPM, it is lowered to the work surface. Unlike high pressure torsion which uses only a few rotations but higher pressure [11], the application of downward pressure and rotation densifies the powder. Figure 3 shows the steps used to fill a hole by HSPC.

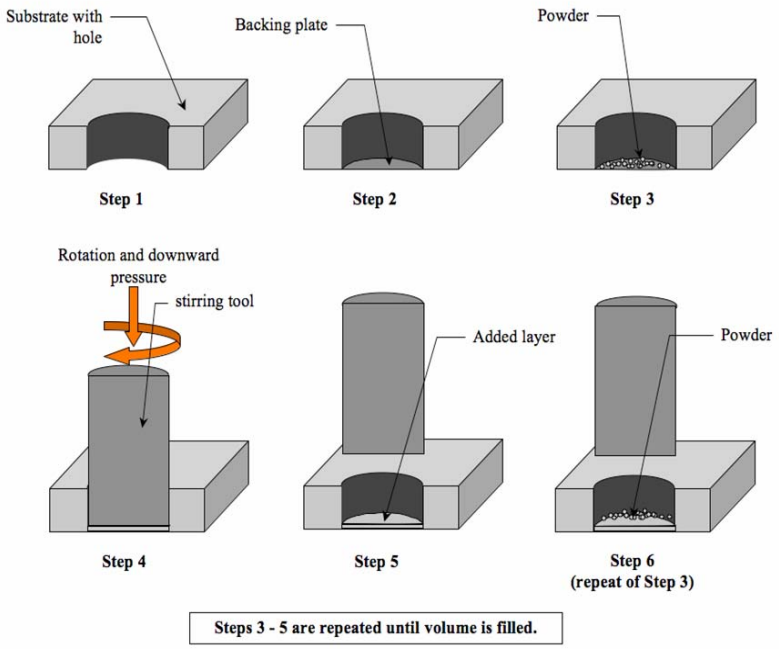

Figure 3: High shear powder consolidation process [19]

There are several advantages to HSPC over other consolidation techniques. Consolidation of the nanocrystalline powder at low temperature is critical to the characterization of these materials. Materials with small crystallites, especially those with high dislocation densities, are very susceptible to recrystallization and grain growth [11, 20]. HSPC offers a solution to this problem by densifying powders at temperatures low enough to prevent crystallite growth and loss of strength [19]. Unlike HIP, HSPC mechanically deforms the powder particles, breaking up the oxide films on the surfaces of the powder particles [21]. These fragmented films are dispersed along the crystallite boundaries and serve to strengthen the material [21].

2.3 X-Ray Diffraction of Crystalline Materials

X-ray diffraction is a tool that can be used to determine crystallite size and lattice strain in a material. When a crystalline material is irradiated with x-rays, some of the x-

rays are reflected by crystal planes. The intensity of this reflection is measured by the diffractometer's detector, resulting in a diffraction peak. The ideal peak shape is one without any width (i.e. a line). Broadening of the diffraction peaks can be traced back to determine crystallite size and lattice strain in a material. Typically, a peak's width is measured at half of its maximum intensity, or "full width at half max" (FWHM). Peak broadening can be attributed to three different factors: instrumental effects, crystallite size, and lattice strain [7, 8]. The instrumental effects vary with each diffractometer and are caused by imperfect measurement capabilities, such as unfocused beams and unresolved α_1 and α_2 peaks [8]. It is necessary to quantify the instrumental broadening of the diffractometer so that the effects of crystallite size and lattice strain can be individually identified in the diffraction patterns of experimental samples.

In mechanically alloyed powders, small crystallite sizes and microstrain contribute to peak broadening [10]. The crystallites in a material are slightly misoriented with respect to each other, and therefore reflect the x-rays at slightly different angles. Having too few atomic planes per crystallite causes the width of the diffraction peak to increase [7, 22]. Lattice strain, which can either be elastic or plastic, is caused by a combination of mechanical work, chemical composition, defects, and stacking faults [8, 23]. During cold work, a crystallite is plastically deformed. As slip occurs during deformation, the crystallites change shape. However, each crystallite remains constrained by its surrounding crystallites, thus contributing to a residual elastic stress in the material. Because each crystallite is deformed differently, the internal strain is nonuniform throughout the material and contributes to a broader x-ray diffraction peak

[7]. Figure 4 shows a schematic of how a diffraction peak is affected by the three factors discussed.

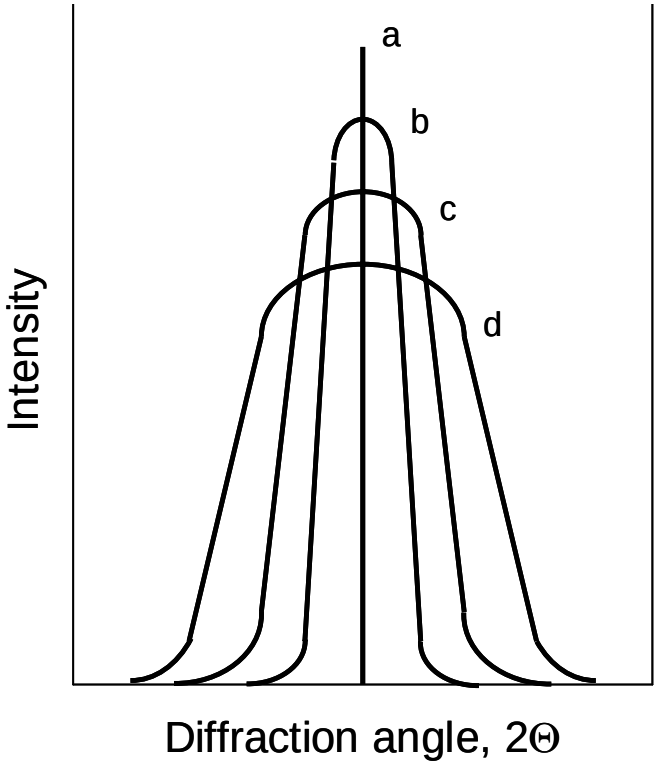

Figure 4: X-ray diffraction peak widths: (a) ideal, (b) due to instrumental effects only, (c) instrumental and crystallite size effects, and (d) combined effects of instrumental, crystallite size, and lattice strain (not to scale)

In order to identify the contributions of crystallite size and lattice strain on the peak broadening, the instrumental effect must first be quantified. The x-ray diffraction pattern of a standard calibration crystal is used to reveal the peak broadening of a specific diffractometer due to instrumental effects. By subtracting the instrumental broadening effect from the diffraction pattern of a material sample, the remaining widths of the diffraction peaks are attributed to the small crystallite sizes and lattice strains [8].

The observed x-ray diffraction pattern of a material sample has a peak of width B_0

$$B_0 = B_i + B_{crystallite} + B_{strain} \tag{3}$$

where the broadening due to instrumental effect, crystallite size, and lattice strain are B_i, $B_{crystallite}$, and B_{strain}, respectively. After subtracting the peak broadening due to the instrumental effect, the width of the diffraction peak, B_r, was considered to be

$$B_r = B_{crystallite} + B_{strain} \tag{4}$$

The peak broadening resulting from small crystallite sizes, $B_{crystallite}$, is represented by the Scherrer equation [7, 8] as

$$B_{crystallite} = \frac{k\lambda}{L \cdot \cos\theta} \tag{5}$$

where θ is the Bragg angle, L is the average crystallite size, k is a constant, and λ is the wavelength of the x-rays. The Scherrer equation is based on the assumptions of Gaussian peak profiles when diffracting small cubic crystallites of uniform size, using a k-value of 0.94 [8]. Because this equation is now also used to determine crystallite sizes of non-cubic materials, k can vary between 0.89 and 1.39. However, since the precision of crystallite size using the Scherrer formula is $\pm$10% at best, k is typically taken as 1.0 [8]. The peak broadening attributed to lattice strain, B_{strain}, is

$$B_{strain} = \eta \cdot \tan\theta \tag{6}$$

where η is the strain in the material [22]. Physically, strain is quantified by measuring the systematic variation in the peak width caused by nonuniform lattice spacing. Substituting into equation 4 gives the width of the diffraction peak, B_r, due solely to crystallite size and lattice strain as

$$B_r = \frac{k\lambda}{L\cos\theta} + \eta \cdot \tan\theta \tag{7}$$

This equation is applied to the peaks in the diffraction pattern and solved for crystallite size, L, and strain, η.

3 Chapter Three – Experimental Procedure

Several techniques were used to characterize the metal powders that were the result of the cryomilling process. This chapter describes the equipment and procedure used for cryomilling and consolidation, as well as each method of characterization to the extent that would allow the reader to perform these techniques in a laboratory.

3.1 Attritor Conversion to Cryogenic Cooling

A Union Process® Szegvari Attritor System® was modified from having water-cooling via a jacket to have cryogenic cooling capabilities. The attritor used in this experiment was model 01HDT having a Reeves motor rated to 0.25 hp. Cryomilling, as the name describes, is ball milling performed in a bath of liquid nitrogen. An open-loop system was designed and constructed to deliver the liquid nitrogen.

A 160-liter, 152 kPa (22 psi) cylinder of liquid nitrogen was used for all experiments. A regulator was used to reduce the inlet pressure from 152 kPa (22 psi) down to approximately 34.5 kPa (5 psi). A pressure-release valve and pressure gauge were also used in line with the cylinder to regulate the liquid nitrogen flow. To directly control the flow of liquid nitrogen into the attritor can, a cryogenic solenoid valve was mounted in line with the liquid nitrogen tank. A thermocouple was threaded through the lid of the attritor can to measure the internal temperature. The thermocouple was linked to a temperature controller, which was also wired to the solenoid valve in such a way that when the temperature inside the can rose above the set point, the valve was opened to

allow liquid nitrogen to flow. Table 1 lists the specifications of the components used in this system, which is shown in Figure 5.

Table 1: Cryogenic conversion attritor components

Part	Component	Description
A	Attritor	Union Process 01HDT
B	Attritor can	1400 cm^3, stainless steel
C	Omega® thermocouple	model: TEX-SEFE-T-3/4-6
D	Solenoid valve	cryogenic brass valve, 0-414 kPa (0-60 psi)
E	Eurotherm© controller	model: 2416
F	Pressure gauge	2" dial gauge, 0-690 kPa (0-100 psi)
G	Pop-safety valve	adjustable brass valve, 41.4-103 kPa (6-15 psi)
H	Regulating valve	2-way brass valve, 13.8-103 kPa (2-15 psi)
J	Liquid Nitrogen	152 kPa (22 psi) cylinder

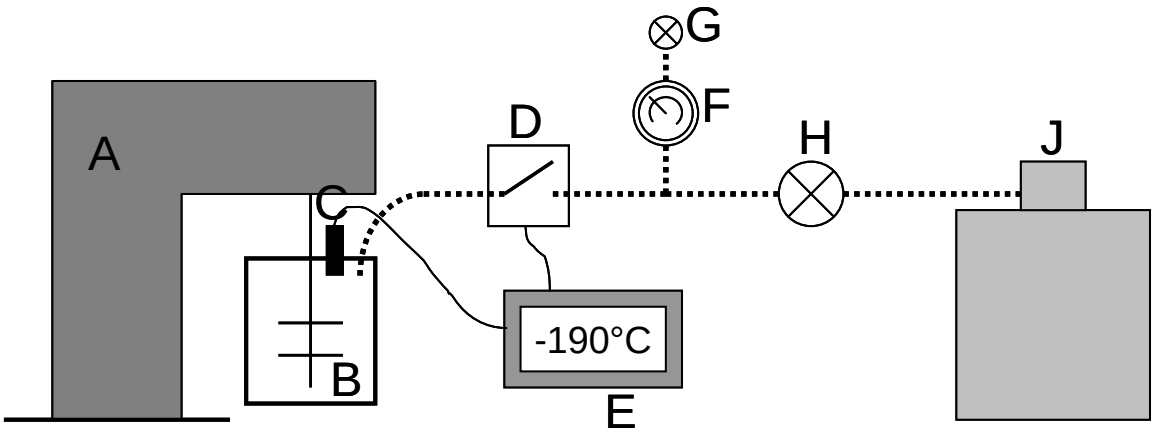

Figure 5: Diagram of attritor with cryogenic cooling

3.2 Selection of an Alloy System

A series of Al-Mg and Mg-Al model alloys were selected for this study. The solubility of one element in the other was considered. A maximum equilibrium solid solubility of greater than 10% was desired to ensure that an alloy would be formed. Figure 6 shows the aluminum-magnesium phase diagram. The maximum solubility of magnesium in aluminum is 17.1%, while aluminum has a maximum solubility of 12.9% in magnesium [24].

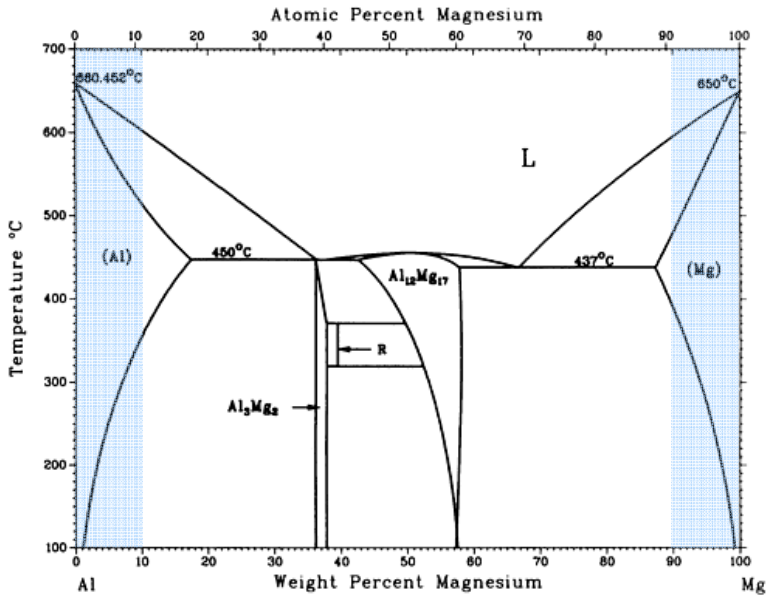

Figure 6: Aluminum-magnesium phase diagram [24]. Reprinted with permission of ASM International®. All rights reserved. www.asminternational.org

The Hall-Petch relationship describes the strengthening in metals as a function of crystallite diameter, d, according to

$$\sigma_{ys} = \sigma_o + k_y \cdot d^{-1/2} \tag{1}$$

For elemental aluminum, the value of k_y is reported as 0.068 MN/m$^{3/2}$, and 0.279 MN/m$^{3/2}$ for magnesium [25]. Thus, even though the Hall-Petch constants are likely valid only for materials of conventional grain sizes, they nonetheless provide guidance as to the relative response anticipated for Al-rich and Mg-rich alloy variants with nanoscaled crystallites that evolve during cryomilling.

Compositions of 0, 4, 7, and 10 wt.% alloying elements were studied. As shown in Figure 6, all compositions fall within the single-phase regions of the Al- and Mg-solid solution phase fields, albeit at elevated temperatures. All exceed the equilibrium solid solubility at room temperatures.

Figure 7 and Figure 8 show scanning electron microscopy (SEM) images of the as-received powders. The aluminum used in this study was -325 mesh, spray-atomized powder, listed as 99.9% pure (Atlantic Equipment Engineers, Bergenfield, NJ), while the magnesium used was -50/+100 mesh spray-atomized powder, listed as 99.8% pure (Atlantic Equipment Engineers, Bergenfield, NJ). Other SEM images of the as-received powders can be found in Appendix A.

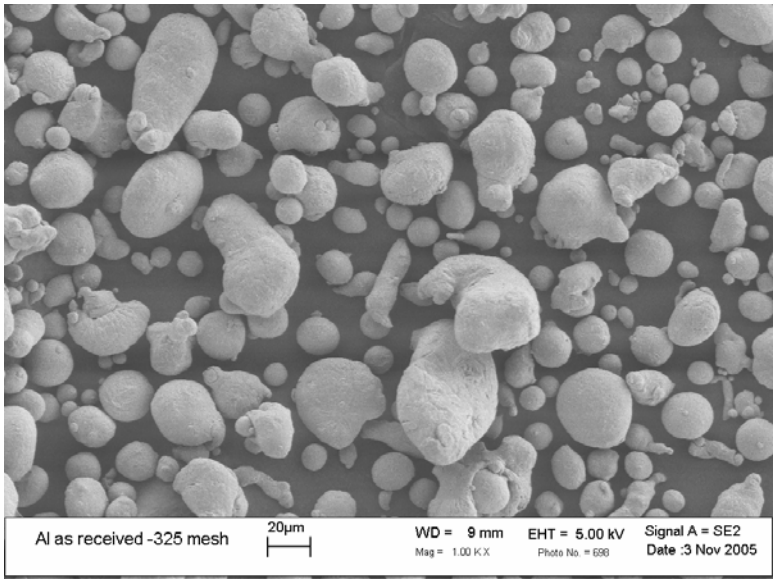

Figure 7: Scanning electron micrograph of as-received Al powder

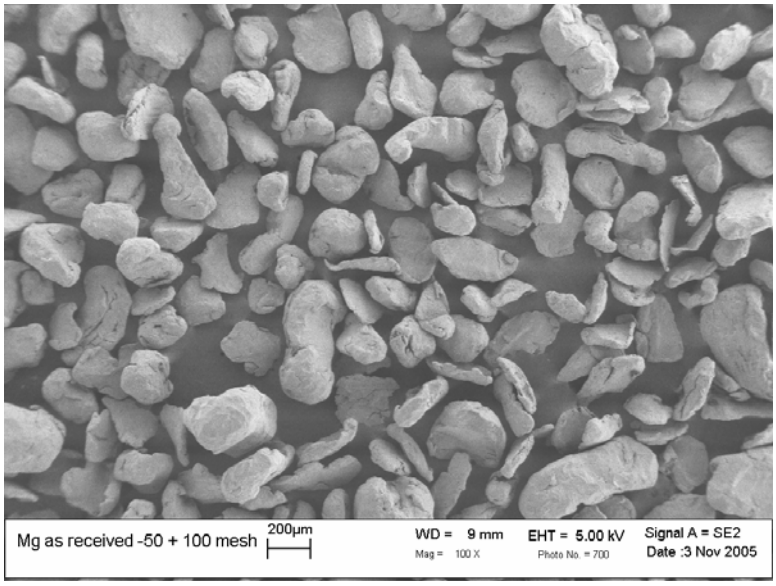

Figure 8: Scanning electron micrograph of as-received Mg powder

3.3 Cryomilling

A stainless steel vessel and impeller, along with 3636 g (8 lb) of stainless steel milling media measuring 6.35 mm (¼ in) in diameter, were used in the milling process. Figure 9 shows a schematic of the interior of the attritor can with the impeller and milling media. The powder occupies the space in between the milling media.

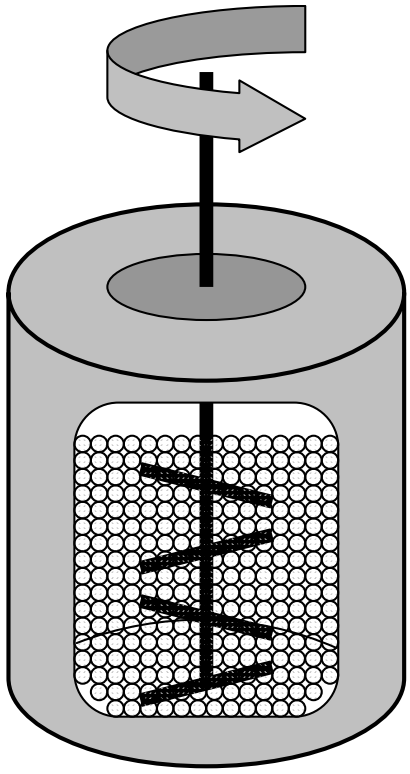

Figure 9: Diagram of the inside of the attritor can

Using a charge ratio of 32:1 (mass of milling media : mass of powder), each batch consisted of 113.64 g of powder. A series of Al-*x* wt.% Mg and Mg-*x* wt.% Al (*x* = 0, 4, 7, 10) samples were prepared, one at a time, using the elemental powders. The powders were mixed in a beaker with 0.25 wt.% stearic acid, which served as a lubricant to prevent cold welding of the powder to the milling media [1, 2, 6].

The system was cooled to -150°C with the attritor running at 110 RPM. The motor and flow of liquid nitrogen were then stopped, the powder was poured into the attritor can using a funnel, and the system was restarted. The temperature controller was set at -190°C to ensure that the milling media remained immersed in the liquid nitrogen bath. The powder samples were cryomilled at 200 RPM for either 4 or 8 hours.

The powder was separated from the milling media using a sieve. The mass of the powder collected was weighed to determine the process yield. Samples were stored in plastic vials at room temperature.

3.4 Pycnometry

A gas displacement pycnometer was used to measure density of the as-received, as-milled, and milled-and-alloyed powders. The Micromeritics® AccuPyc 1330 uses the ideal gas law to calculate the volume of solid material in the sample cup. After calibrating the pycnometer with the 1 cm^3 cup and inputting the sample mass, the cell chamber is filled with helium gas to a set elevated pressure. The pycnometer measures the change in pressure of the helium when it is allowed to equilibrate between the cell and expansion chambers to find its volume. The sample volume is now known, and is divided by its mass to find density. The process is cycled ten times to generate multiple measurements and find an average density. The derivation for the calculation to analyze density can be found in Appendix B. Figure 10 shows a diagram of the pycnometer chambers.

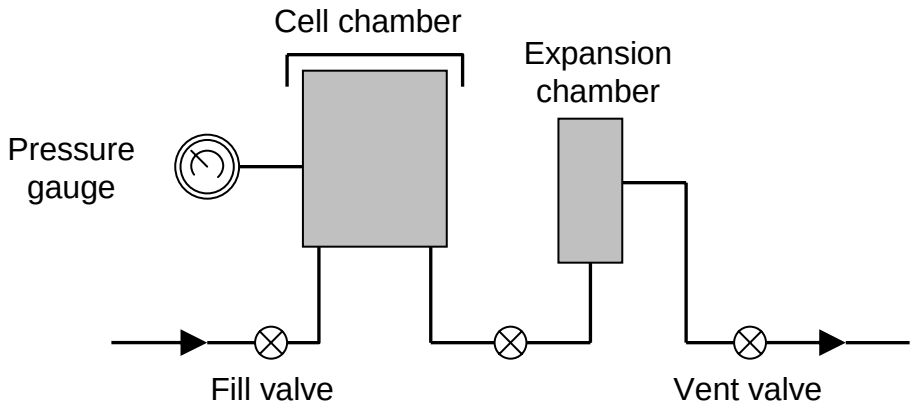

Figure 10: Diagram of gas displacement pycnometer

3.5 High Shear Powder Consolidation

High shear powder consolidation (HSPC) was used to densify a select subset of all the powder materials used in this experiment. After machining a 0.953 cm (0.375 in) diameter hole 0.254 cm (0.1 in) deep in a block of 5083 aluminum, approximately 0.25 g of the sample powder was added to the hole. With the 0.953 cm (0.375 in) diameter stirring tool rotating at 3500 RPM, downward pressure was manually applied. The stirring tool was raised and the process was repeated until the densified powder material was level with the block. Figure 3 in Chapter Two shows the steps of the HSPC process.

3.6 Hardness Measurements of Consolidated Samples

The consolidated powders were cut from the aluminum block and sectioned in half using a water-cooled abrasive cut-off wheel. Each sample was mounted in epoxy and standard metallographic techniques were used to achieve a polished surface.

Hardness measurements were done using a Vickers microhardness test machine. A load of 200 g and a dwell time of 15 sec were used. Five measurements were taken across the face of the consolidated samples, and the values are reported as an average with error bars showing the standard deviation.

The hardness could not be directly determined from as-received or as-milled powder particles. Mounting powder in epoxy and forming discs of powder in a compaction die proved unsuccessful because the localized pressure of the hardness indenter displaced surrounding material, leading to inaccurate measurements. Thus, hardness was only measured on consolidated samples.

3.7 X-ray Diffraction

All x-ray diffraction measurements were conducted in the High Temperature Materials Laboratory at Oak Ridge National Laboratory with assistance from Dr. Andrew Payzant. X-ray diffraction was performed using a Philips PANalytical X'Pert Pro Multi-purpose diffractometer equipped with an X'celerator detector. The diffractometer had a programmable divergence slit with a 0.04 rad Soller and a 0.5-degree divergence slit on the Cu Kα x-ray source. A 10-mm mask was used to limit the beam width on the axial side in combination with an anti-scatter slit measuring 0.5 degrees. The samples were placed on a multi-purpose sample stage with adjustable height. A 0.5-degree anti-scatter slit, 0.04-rad Soller, and nickel thin film filter were mounted on the detector. The x-ray patterns were collected at -45 kV and 40 mA, in the range of 30-141 degrees with a step size of 0.167 degrees and at a rate of 20 sec per step.

3.7.1 Determination of Crystallite Size and Strain

X-ray analysis software was used to interpret the data. HighScore Plus (Panalytical) is a powerful platform used for pattern processing by the Rietveld method. Jade, version 6.5 (Materials Data, Inc.), calculates crystallite size and strain in the material using equation 7 presented in Chapter Two.

The x-ray diffractometer was calibrated by measuring a single crystal of lanthanum hexaboride (LaB_6), a commonly used NIST-certified calibration standard. Figure 11 shows the diffraction pattern for LaB_6, which was used to characterize this instrument's effect on peak broadening.

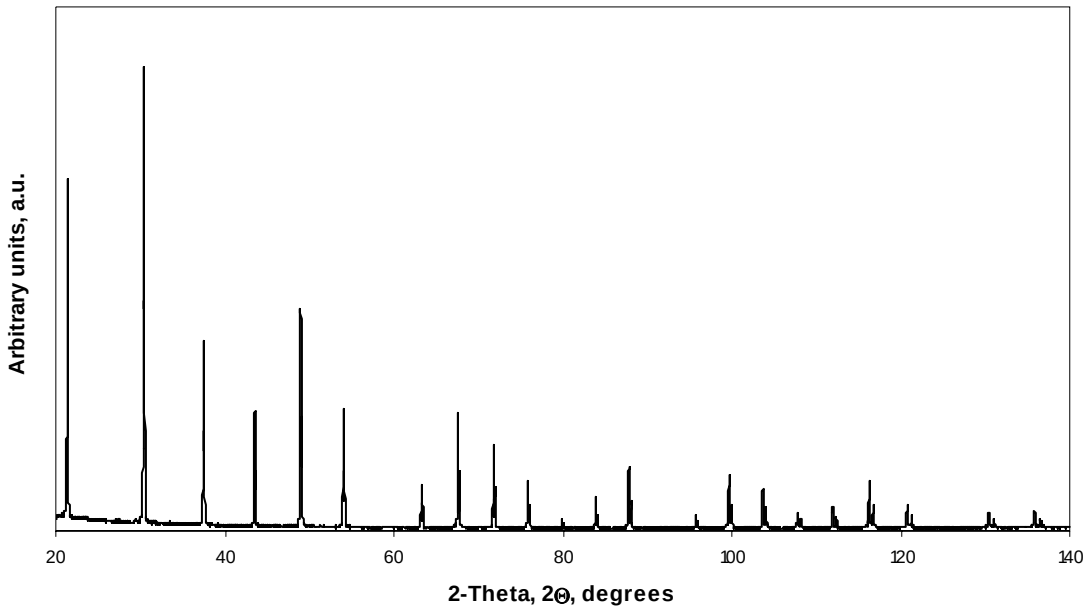

Figure 11: X-ray diffraction pattern of LaB_6 standard

After subtracting the peak broadening due to the instrumental effect, the width of the diffraction peak was attributed to crystallite size and lattice strain (equation 4, p. 14). HighScore Plus takes into account instrumental effect and uses the Rietveld method to refine a structure model to the full diffraction pattern. The Rietveld method allows atomic position, fractional occupancies, and displacement parameters to refine in order to optimize a profile to the observed diffraction pattern [26]. Additionally, absorption and extinction terms are allowed to correct while unit cell constants, peak shape, and asymmetry parameters are refined to improve profile fit [26].

The formula used by Jade to calculate crystallite size and strain was given on page 14. Using a Williamson-Hall plot, the crystallite size and strain in the material were calculated by plotting of peak width (FW) times cosine θ versus sine θ. By equation 7 (p. 14), the slope of the line represents the microstrain and the intercept gives the crystallite size. Figure 12 shows the Al 4 hr mill sample as an example of this type of plot, with the

calculated crystallite size (XS) and lattice strain values listed at the top of the figure. The Williamson-Hall method is often used for this purpose [27, 28].

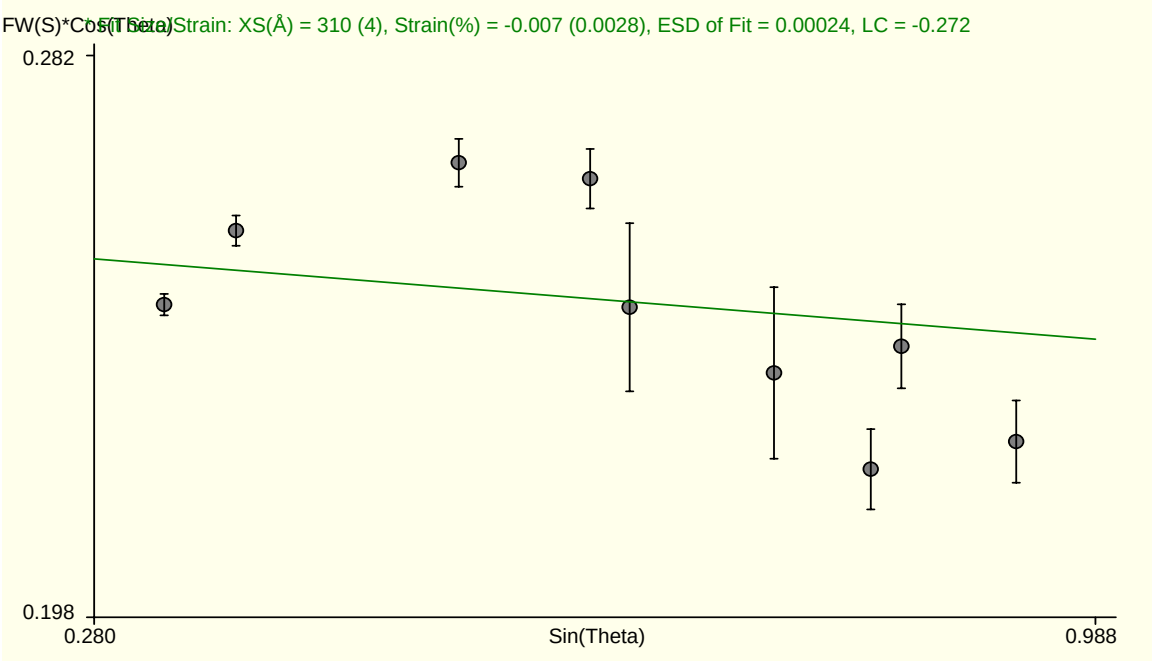

Figure 12: Williamson-Hall plot example, Al 4 hr mill

4 Chapter Four – Results and Discussion

This chapter reports the results of the experiment and provides explanations for the trends observed. The four major sections of this chapter are presented in order of increasing importance.

4.1 Powder Yield Following Cryomilling

The amount of powder that could be cryomilled was dependent on both the size of the attritor can and the charge ratio. Using a 32:1 charge ratio, 113.64 g of powder could be milled in each batch. The amount of this powder that was collected post-processing was of interest for two reasons. Fundamentally, the process yield was important for the purposes of refining and improving the newly modified attritor system. Secondarily, when creating alloys by cryomilling, it was necessary to confirm that a significant portion of the metal powder was not lost. In the event of considerable loss during cryomilling, the relative compositions of the elemental powders, whether it be 4, 7, or 10 wt.%, would not be accurate. Obviously, a low yield for a pure, unalloyed batch is of less concern from a scientific point of view.

The loss of powder during cryomilling turned out to be a greater problem than was anticipated. While leaky seals allowed some powder to escape, the bigger culprit was determined to be pressure build-up inside the attritor can. The pressure of the liquid nitrogen as it entered the can was thought to create turbulence in the liquid nitrogen bath. This turbulence was enough to splash liquid up and into the tubes designed to vent the nitrogen gas as the liquid evaporated. Since the liquid nitrogen bath contained the

powder particles, they too were carried into the vent tubes. The pressure generated in the headspace by the evaporation of the liquid pushed this powder up and out of the vent tubes. Losses were significant in some cases, ranging from 21% to 81%.

Control of the inlet pressure was carefully monitored so as to find an inlet pressure great enough to maintain a temperature below -190°C but also limit the loss of powder through the vent tubes. A curved copper tube was also added to the liquid nitrogen inlet port directing the flow in a clockwise direction, complementing the rotation of the impeller. This reduced the turbulence inside the can and decreased the powder loss. Table 2 and Table 3 compare the powder yields before and after the addition of the copper tube.

For the purposes of this study, a minimum yield of 75% was considered acceptable for alloyed materials, and those samples were further characterized. For pure samples, lower yields were deemed tolerable, and therefore not rejected from further study. The asterisks (*) next to the alloy indicate which materials were selected for further study and processing.

Table 2: Powder yield without copper tube

Alloy	Milling time (hr)	Yield (%)
Al	4	22.1
Al*	4	67.1
Al	8	18.3
Al*	8	65.0
Al-4 wt.% Mg*	4	78.7
Al-7 wt.% Mg	4	42.5
Al-7 wt.% Mg	4	54.7
Al-10 wt.% Mg	4	53.5

Table 3: Powder yield with copper tube

Alloy	Milling time (hr)	Yield (%)
Al-7 wt.% Mg*	4	90.9
Al-10 wt.% Mg*	4	97.4
Mg*	4	98.3
Mg-4 wt.% Al*	4	97.2
Mg-7 wt.% Al*	4	100#
Mg-10 wt.% Al*	4	93.1

- Sample was damp when weighed

4.2 Powder Density

The densities of both the as-received and cryomilled powders were measured using pycnometry. The density of pure Al is 2.70 g/cm^3, while that of Mg is 1.74 g/cm^3 [29]. Figure 13 and Figure 14 show the plots of powder density versus alloy composition. The red data points represent the as-received powder, while the green points denote published values of the bulk densities of commercial alloys having either Mg or Al as the main alloying element [30]. Pycnometry uses helium gas to measure sample volume, and therefore would not account for internal voids or porosity. Thus, the values reported are apparent densities.

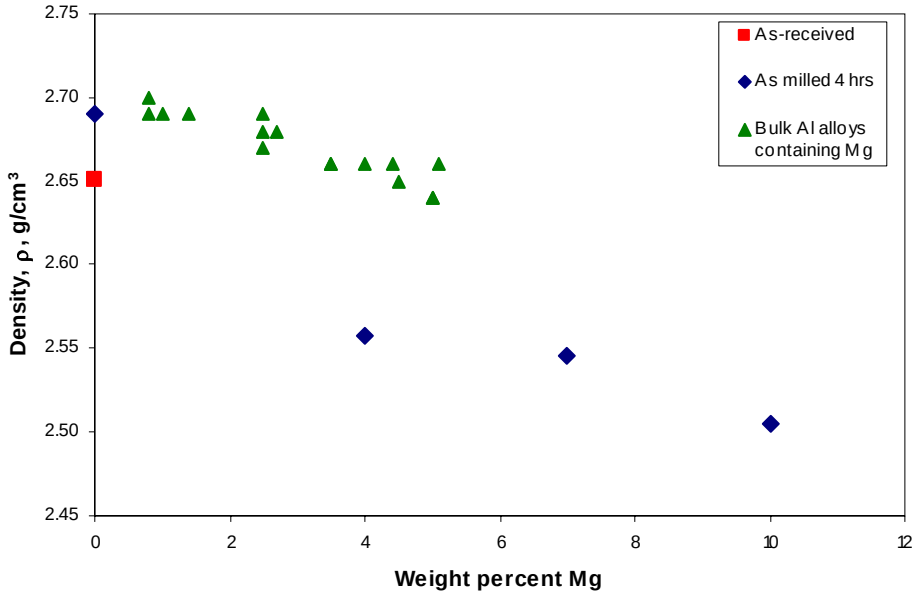

Figure 13: Density versus weight percent Mg for Al alloys

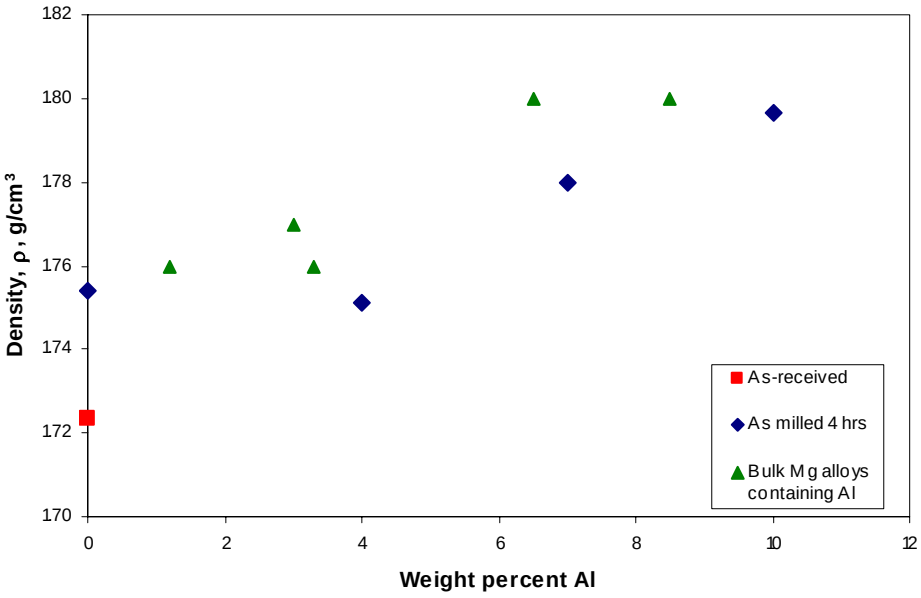

Figure 14: Density versus weight percent Al for Mg alloys

The general trends in this data confirm the presence of an alloying element. The density of the Al-rich samples decreases with increasing Mg content, as expected.

Similarly, the density of the Mg alloys increases with Al content. The observed changes in density are considered to be predominantly caused by alloy content. It is interesting to note the increase in density from the as-received condition to the as-milled condition. This increase could indicate small levels of porosity in the unprocessed powder, although no evidence or literature has been found to this effect.

The Al-rich alloys were found to be slightly less dense than comparable wrought alloys; however, the densities of the Mg alloys were consistent with the bulk materials containing Al. This variance can be attributed to the presence of other elements in the commercial alloys. The most common elements alloyed in Al-Mg wrought materials (5xxx series) are Mn and Cr [30]. Other elements such as Si, Fe, Cu, Zn, Ti, V, and Ga are also found in trace amounts [30]. All of these elements have densities greater than that of Al and Mg, which account for differences observed.

4.3 Hardness of Consolidated Powder Samples

The strength of nanocrystalline materials is one of their major desirable properties. A material's hardness is a good indicator of its strength, and thus the Vickers hardness of samples densified by HSPC was measured to compare the strength of as-received with cryomilled powders, and unalloyed versus alloyed samples. Figure 15 shows the Vickers hardness measured for the Al-rich samples.

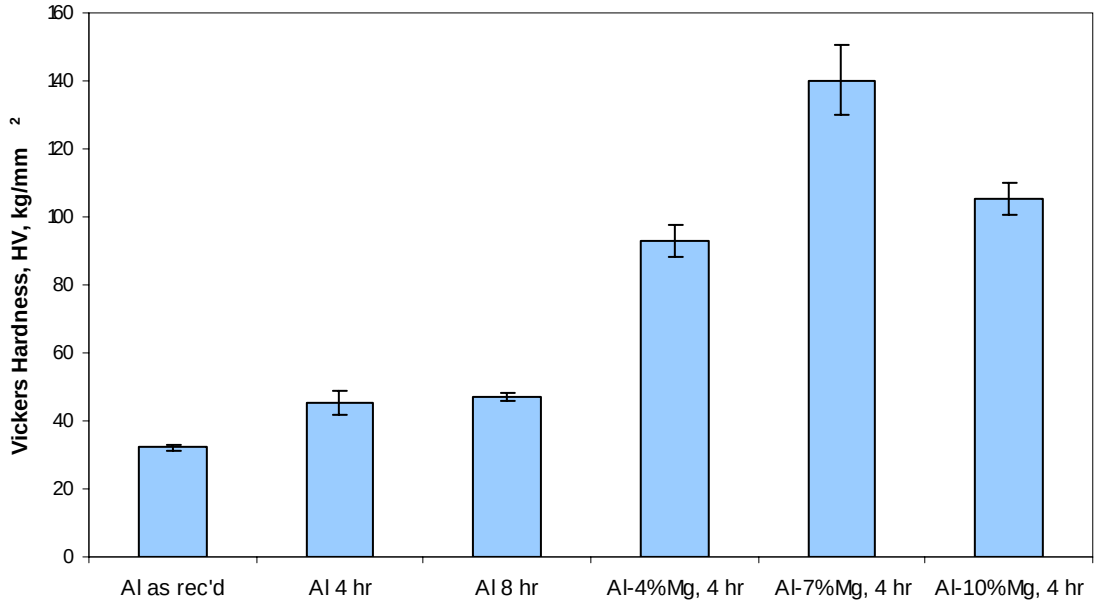

Figure 15: Vickers hardness of Al-rich powders densified by HSPC

The as-received sample had the lowest hardness at 32.2 HV. The effect of cryomilling was a moderate increase in hardness to 45.3 and 47.1 HV for the materials milled for 4 and 8 hours, respectively. These values indicate that milling time does not appear to affect the hardness of consolidated powder. The increase in strength over the as-received material is anticipated as the processed powders contain impurities and interstitials, which strengthen the material [2, 21], and were exposed to severe deformation, introducing a greater dislocation density into the material [6]. When Al was alloyed with Mg during cryomilling, however, a large increase in hardness was observed. Hardness values of 92.8, 140.3, and 105.4 HV were recorded for alloy compositions of 4, 7, and 10 wt.% Mg, respectively. This substantial increase in hardness in the alloyed samples is expected as Mg is known to strengthen an Al matrix across this range of alloy content and cause high work-hardening characteristics [31].

It is interesting to note the occurrence of the maximum hardness in the 7 wt.% Mg sample, and the decrease in hardness when the Mg content increases to 10 wt.%. It would be expected that the 10% alloy has a greater hardness value. An explanation of this peak in hardness at 7% is offered in section 4.4.2.

The Vickers hardness of the Mg-rich samples consolidated by HSPC was also measured. Figure 16 gives the values of this measurement.

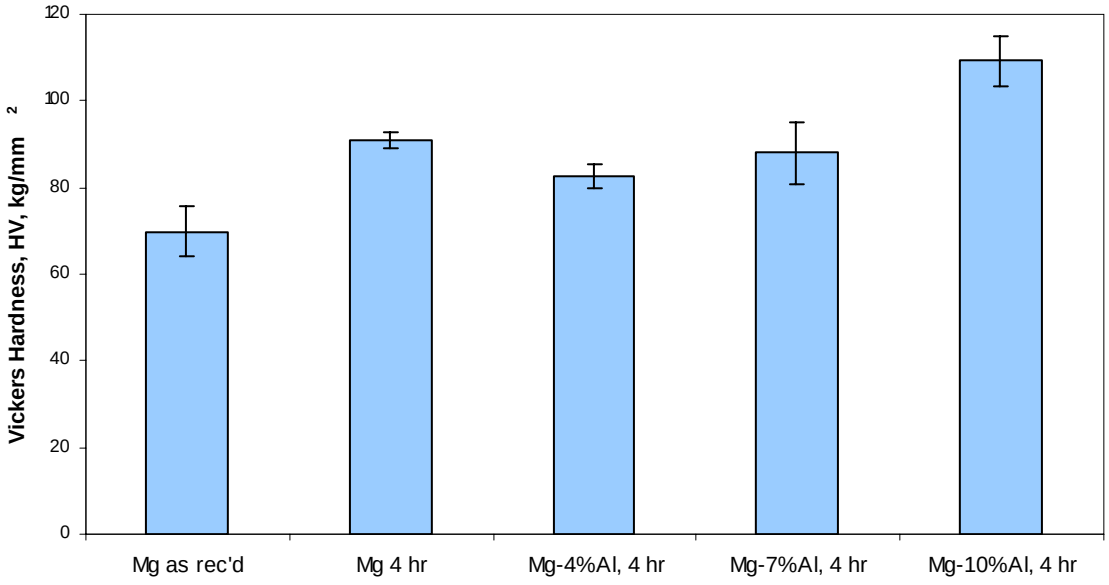

Figure 16: Vickers hardness of Mg-rich powders densified by HSPC

The as-received sample had the lowest hardness at 69.9 HV. The effect of cryomilling was a moderate increase in hardness to 90.9 HV for the material milled for 4 hours. The effect of alloying Al with Mg during cryomilling was incremental increases in hardness with increased alloy content. Hardness values of 82.6, 88.0, and 109.2 HV were recorded for the samples containing 4, 7, and 10 wt.% Al, respectively. This trend is expected as Mg is alloyed with Al for the purposes of improving strength [31].

4.4 Crystallite Size and Strain Analysis by X-ray Diffraction

The size of the crystallites is what makes these materials unique. Nanocrystalline metals produced by cryomilling are commonly characterized by x-ray diffraction in an effort to understand the effect of the process on the crystallite size and strain in the material.

4.4.1 Size and Strain for Powder Samples

Figure 17 shows the diffraction patterns for the four cryomilled Al powder samples. The presence of Mg is confirmed by the small peaks near 34° and 36° in the 7 and 10 wt.% samples.

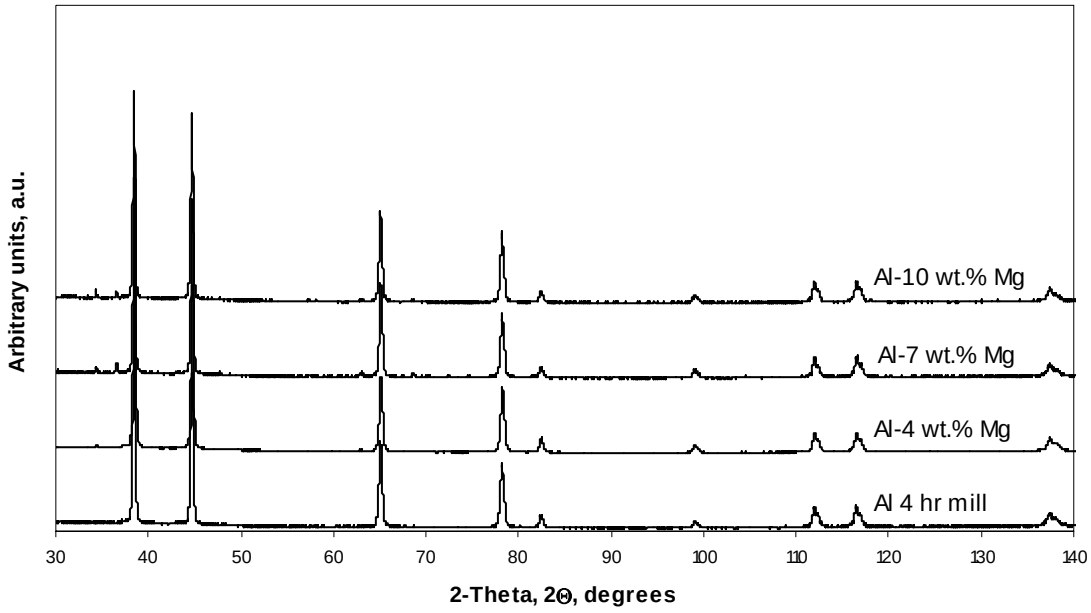

Figure 17: Diffraction patterns of 4-hr mill Al alloy powders

Figure 18 plots the crystallite size and strain, as determined by Jade from the diffraction patterns, for the Al powder samples versus Mg content for samples cryomilled 4 hours shown in Figure 17.

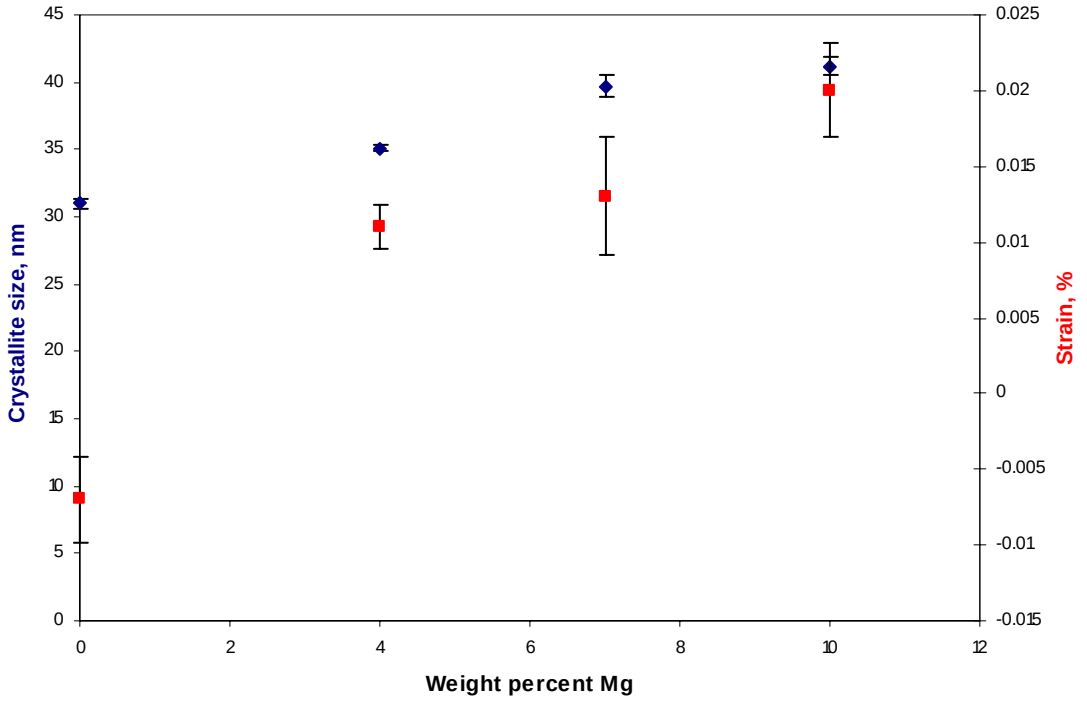

Figure 18: Al crystallite size and strain versus weight percent Mg, 4 hr cryomill

The results show a linear increase in crystallite size from the unalloyed powder at 31.0 nm to 41.2 nm for the Al-10 wt.% Mg sample. In comparison, the crystallite size of the as-received Al powder was found to be 232.8 nm. The reduction in crystallite size of Al is well documented and these size measurements agree with similar experiments found in the literature [2, 6, 10, 11]. Crystallite size has been shown to decrease rapidly with milling time, showing little change with extended milling [5]. This trend was confirmed here as the Al 8 hr mill powder was found to have an average crystallite size of 75.6 nm. Small increases in crystallite size with increasing Mg content are expected as Mg has a larger atomic radius than Al [29]. For the same reason, the strain in the material should increase with greater Mg content. The four samples shown were all cryomilled for 4 hours, and therefore the trends associated with size and strain are due only to the alloy content of the material. In contrast, a cast Al material containing Mg would not have the

same size and strain as a cryomilled sample because it does not undergo the same deformation during processing or have as much Mg in solution.

Figure 19 shows the diffraction patterns for the four cryomilled Mg powder samples.

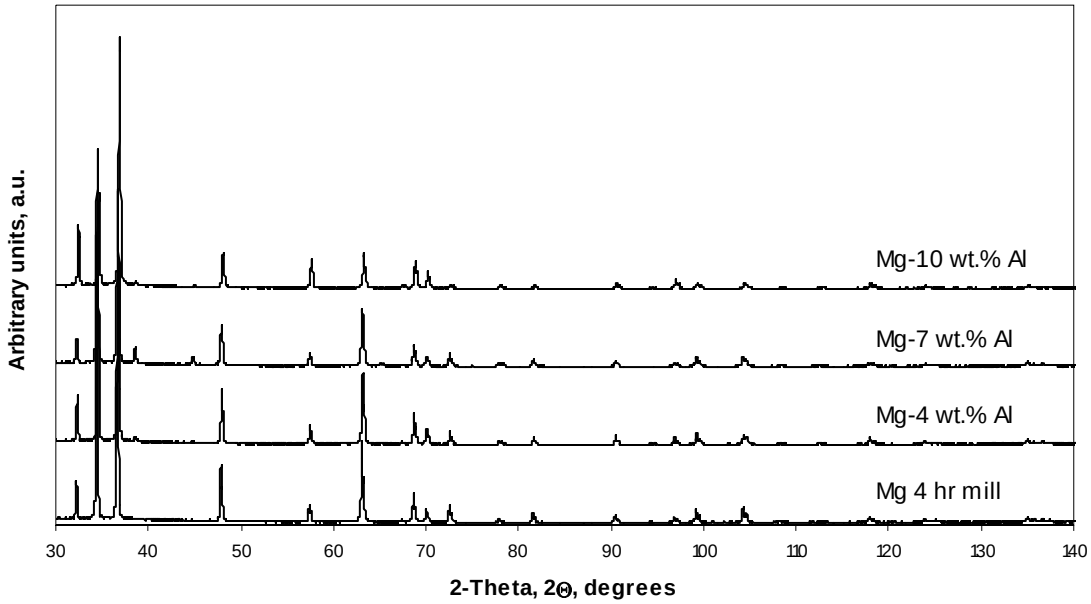

Figure 19: Diffraction patterns of 4-hr mill Mg alloy powders

Figure 20 plots the crystallite size and strain for Mg powder samples versus Al content for samples cryomilled 4 hours shown in Figure 19.

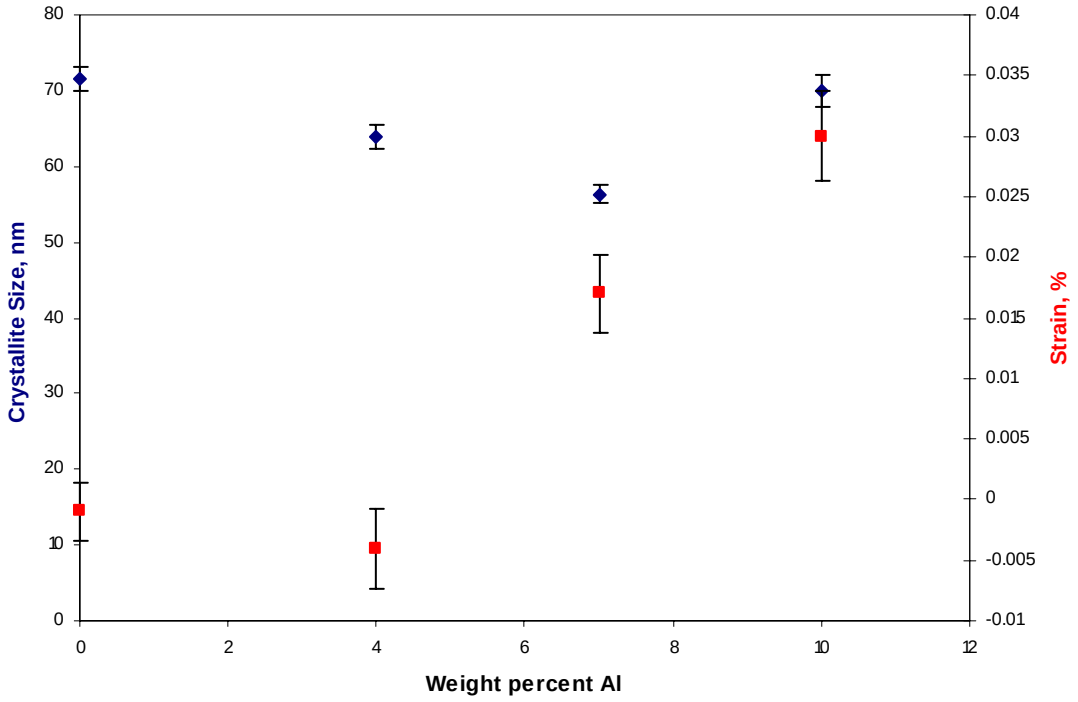

Figure 20: Mg crystallite size and strain versus weight percent Al, 4 hr cryomill

The sizes of the Mg crystallites do not show a definite trend as the amount of Al was increased. The as-received Mg powder had a crystallite size of 69.3 nm, so cryomilling had very little effect on the size. Strain in the material was found to increase with higher alloy content. According to Smith [31], Mg cannot be alloyed with more than about 10% Al or the formation of a brittle intermetallic compound, $Mg_{17}Al_{12}$, dramatically reduces ductility. The higher strains observed in the 7 and 10 wt.% Al samples may be evidence of the presence of this coherent intermetallic. A coherent precipitate this large would strain the lattice considerably, but has been shown to be absent from a diffraction pattern because of this coherency [17].

4.4.2 Size and Strain of HPSC Samples

Figure 21 shows the diffraction patterns for the six consolidated Al samples.

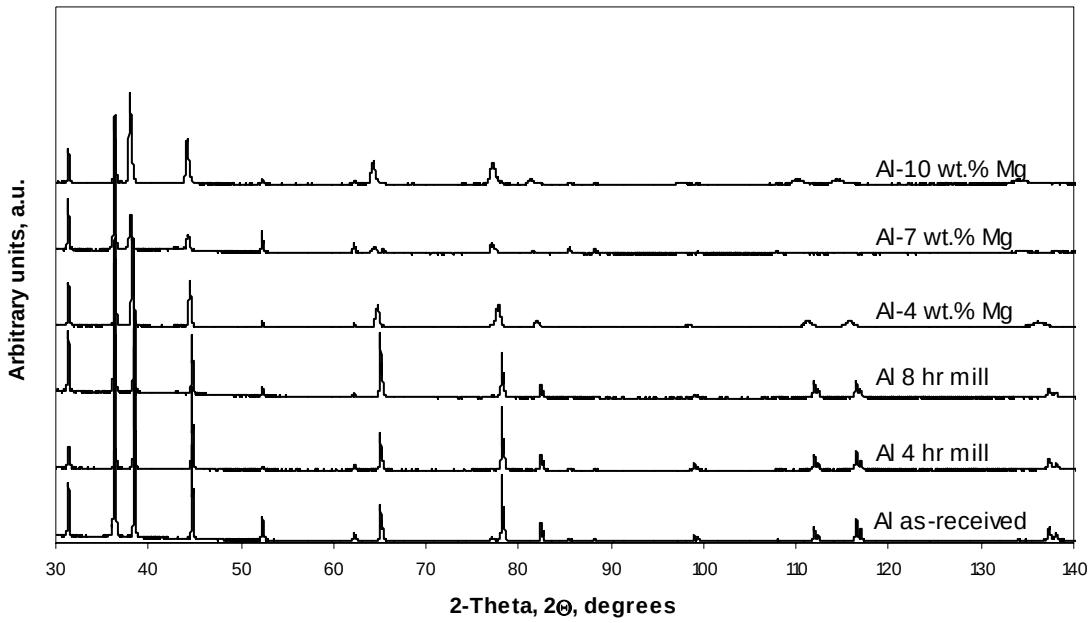

Figure 21: Diffraction patterns of Al HSPC samples

Comparing the diffraction patterns of these six materials, the pattern from the 7% sample is noticeably different from the rest. The peak intensities are smaller, and in some cases peaks are absent. Lower peak intensities are a characteristic of smaller crystallites, which is consistent with the increased hardness measured in Figure 15.

Figure 22 shows the crystallite size and percent strain for the Al samples consolidated by HSPC.

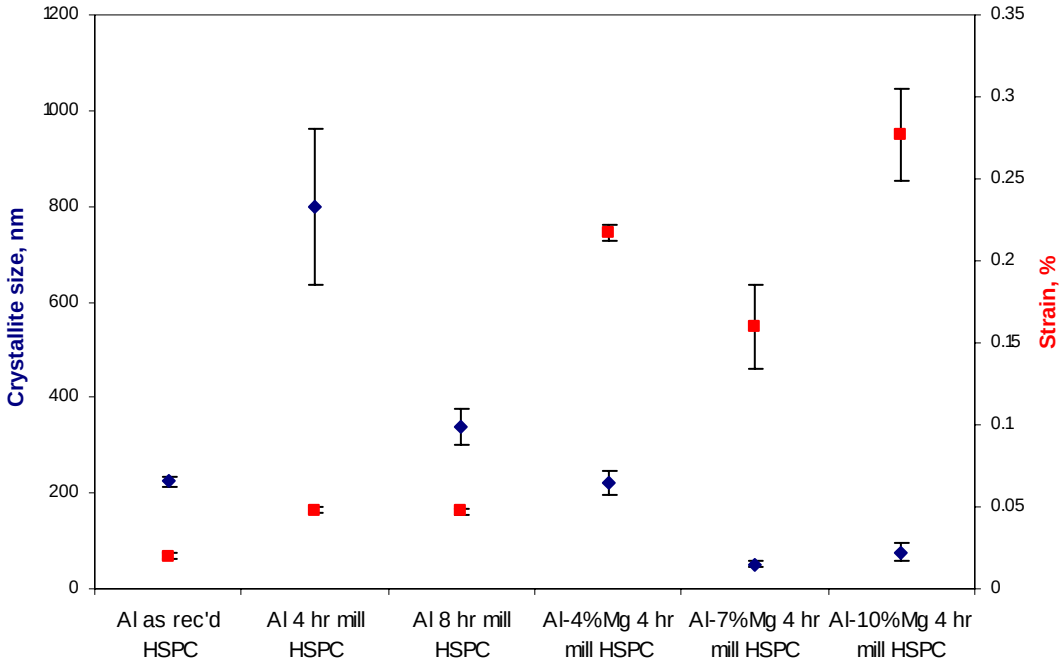

Figure 22: Crystallite size and strain for consolidated Al powders

To this point, these materials have been subjected to severe cold deformation during cryomilling (except as-received) and then high shearing forces during HSPC. Both of these processes contribute to the stored energy in the material. Stored energy comes in the form of lattice defects, such as dislocations, vacancies, and interstitial atoms [16]. The amount of stored energy in a material is affected by its purity, type of deformation, deformation temperature, and crystallite size [16]. This processing history explains why the larger strain values observed in the alloyed samples were an order of magnitude greater than in powder form. Deformation at lower temperatures increases the amount of stored energy because there is less thermal energy to allow the release of the stored energy by interactions between defects [16].

The crystallite sizes measured showed an interesting trend. The as-received powder had essentially the same size before and after HPSC (232.8 nm and 223.7 nm).

The 4-hour mill sample grew significantly from 31 nm in its powder form, as shown in Figure 18, to 800 nm after HSPC. The samples alloyed with 4, 7, and 10 wt.% Mg grew from approximately 40 nm in powder form to 220, 51, and 76 nm, respectively.

Figure 23 shows the diffraction patterns for the five consolidated Mg samples.

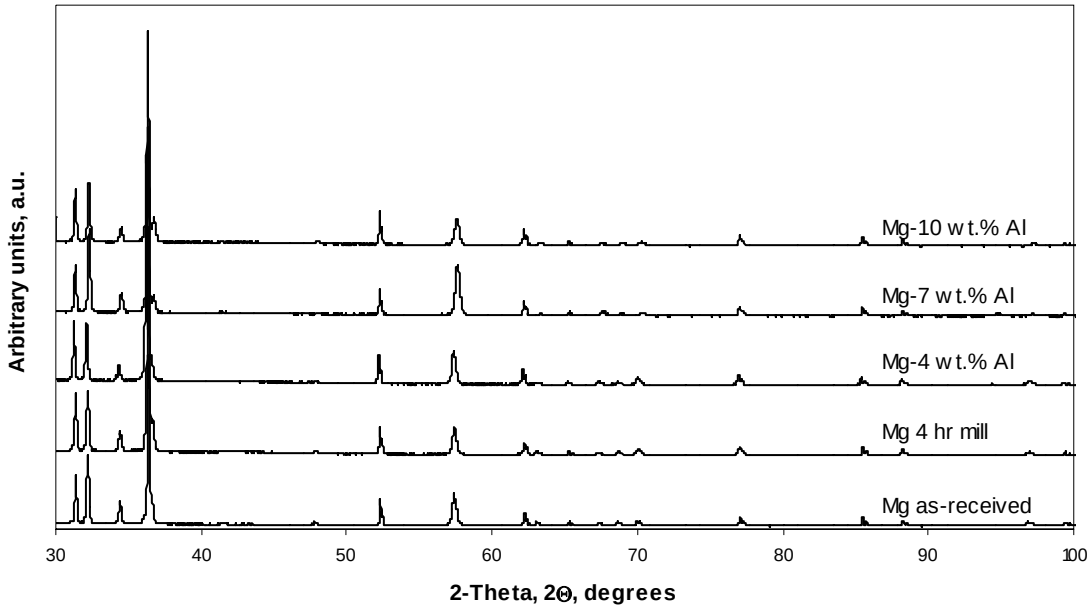

Figure 23: Diffraction patterns of Mg HSPC samples

Figure 24 shows the crystallite size versus percent strain for Mg samples consolidated by HSPC.

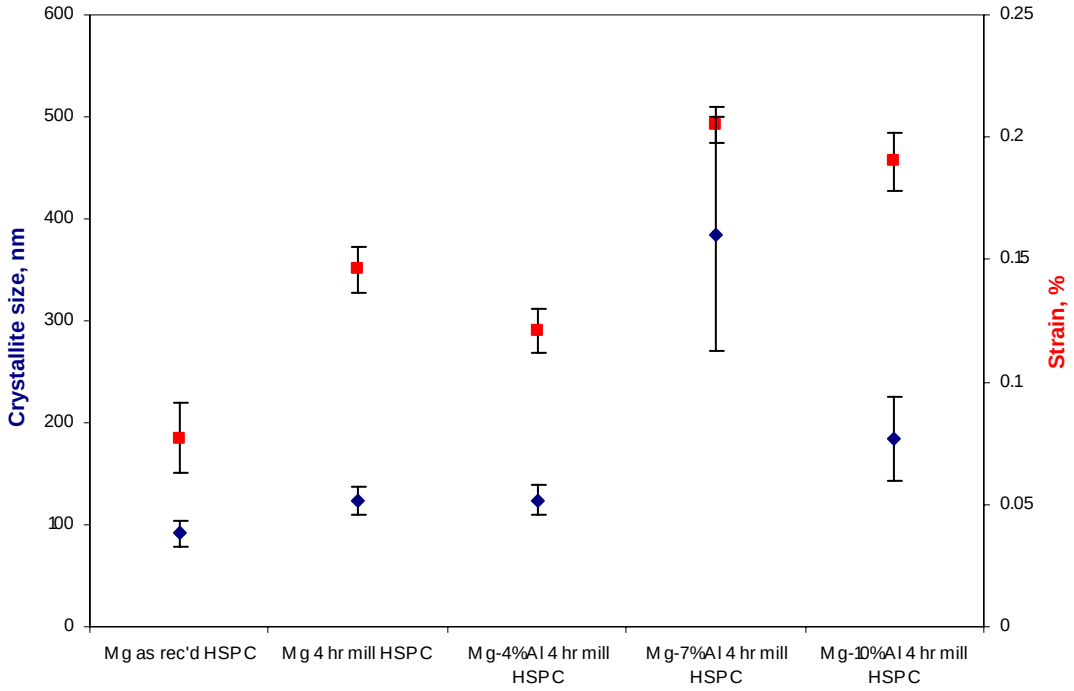

Figure 24: Crystallite size and strain for consolidated Mg powders

The crystallite size was found to increase at higher Al content levels, which is the opposite tendency from what was observed previously in the Al-rich alloys. As shown in Figure 20, the crystallite size of cryomilled Mg powders was between 56 and 72 nm. When consolidated, the 7 and 10 wt.% Al samples were found to have crystallites measuring 385 and 184 nm. During HSPC, it was noted that the Mg alloys seemed to densify quite easily compared to Al, which could be attributed to the fact that the Mg powders were much finer than the Al powders.

4.4.2.1 Dynamic Recovery

The amount of stored energy in these materials makes dynamic recovery a distinct possibility during HSPC. Dynamic recovery is the idea that internal stresses are relieved during mechanical deformation while simultaneously inducing additional internal stresses

(i.e. dislocations) [6, 32]. This theory would explain the larger crystallite sizes and lower strains observed in the as-received and as-milled Al materials. With the addition of heat from friction, the materials could undergo recovery and recrystallization processes. Figure 25 shows illustrations of two models for how the crystallite size (d) might be affected during HSPC.

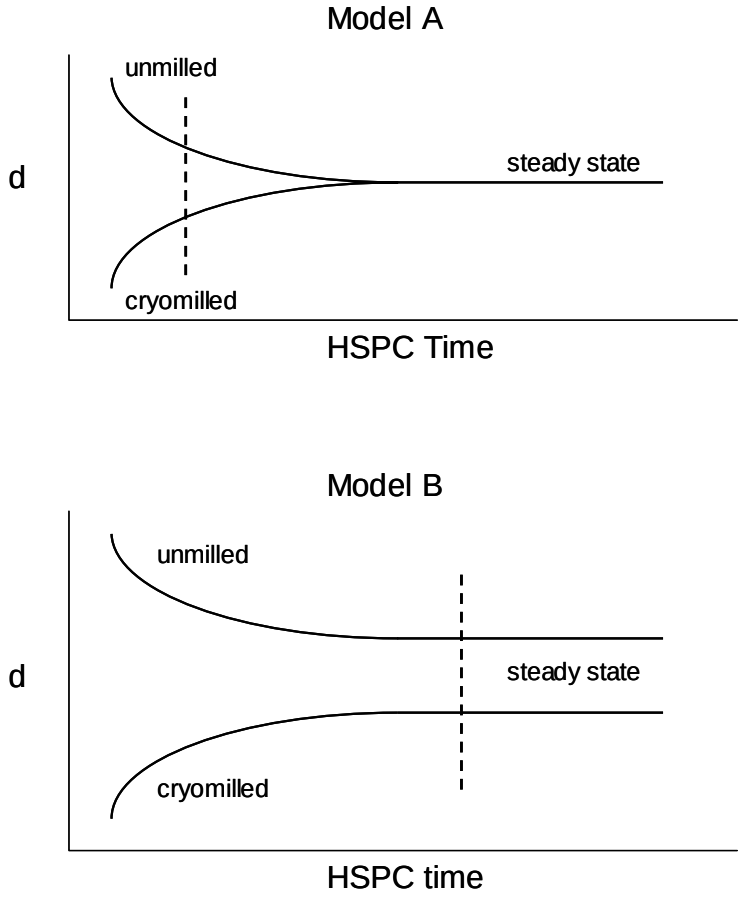

Figure 25: Models of HSPC effect on crystallite size

Both models assume that as-received powders have generally larger crystallite sizes before cryomilling. HSPC breaks down the large crystallites in unmilled materials, but crystallite sizes have been shown to increase in cryomilled powders from HSPC from the heat energy needed to trigger recovery and recrystallization. The steady state shown

in both schematics is reached when recrystallization and grain growth are balanced with the breakdown of the crystallites by shearing.

The difference between the models is the steady state crystallite size of the unmilled versus cryomilled samples. In Model A, the steady state size is the same for both unmilled and cryomilled materials, while Model B shows a variation in the steady state crystallite size. The dashed lines indicate how, for identical HSPC time, there may be observed differences in crystallite size. It is impossible to say which model is correct without extensive further study of this subject.

In the case of the alloyed samples, having Mg present makes recovery more difficult by limiting the mobility of dislocations. The effect of this is two-fold: the material is unable to relieve its lattice strain, and growth of the crystallites is prevented.

4.4.2.2 Vickers Hardness

Figure 26 compares the crystallite size to the Vickers hardness for Al samples consolidated by HSPC. The crystallite sizes decrease from the as-milled state when Mg is added for the reasons explained in the previous section, but this plot also shows a significant increase in hardness with the addition of Mg.

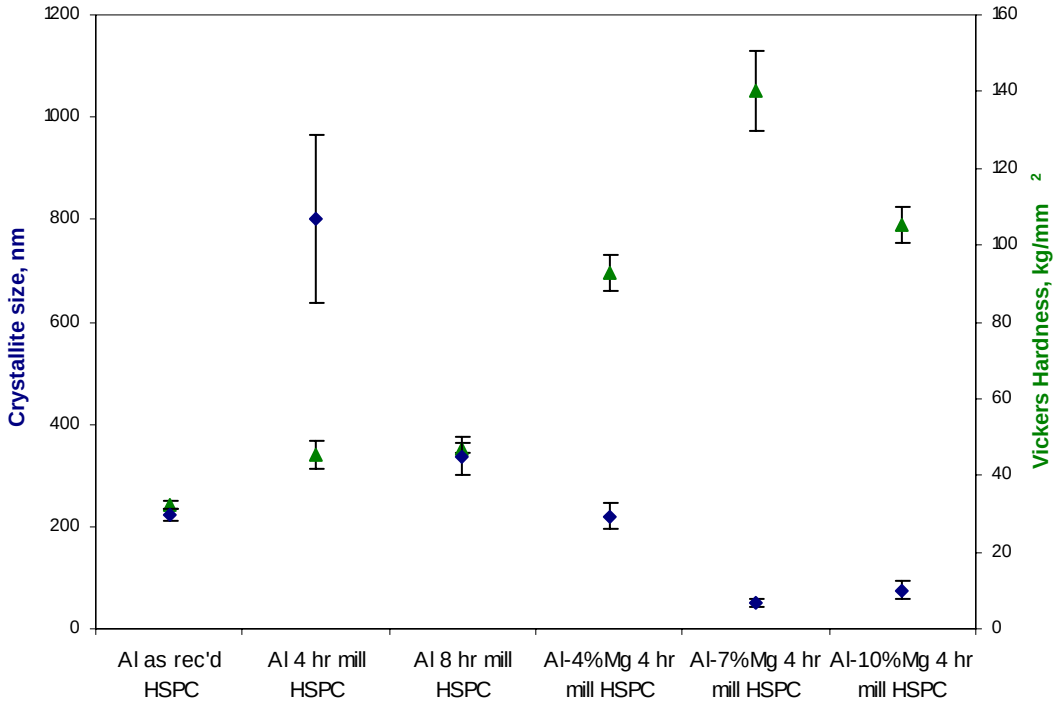

Figure 26: Crystallite size and Vickers hardness for consolidated Al powders

Figure 27, which shows percent strain and Vickers hardness for the densified Al samples, confirms the trend from Figure 26. The hardness curve matches the strain in the material almost exactly. For a material with higher strain (more dislocations, vacancies, impurities) and smaller crystallite size, it is expected to have higher hardness. Conversely, lower lattice strain should correlate to lower hardness, as evidenced by the as-received and as-milled samples.

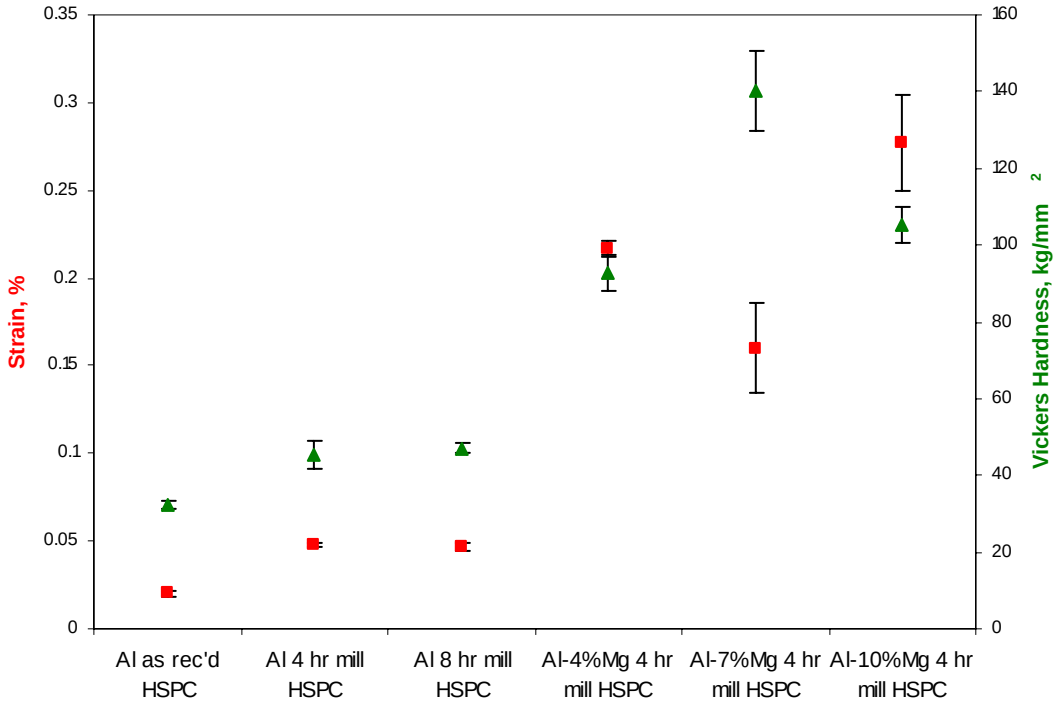

Figure 27: Strain and Vickers hardness for consolidated Al powders

Figure 28 compares the crystallite size to the Vickers hardness, and Figure 29 plots the percent strain and hardness for Mg samples consolidated by HSPC. These plots show trends similar to those observed in the consolidated Al samples in terms of strain and hardness.

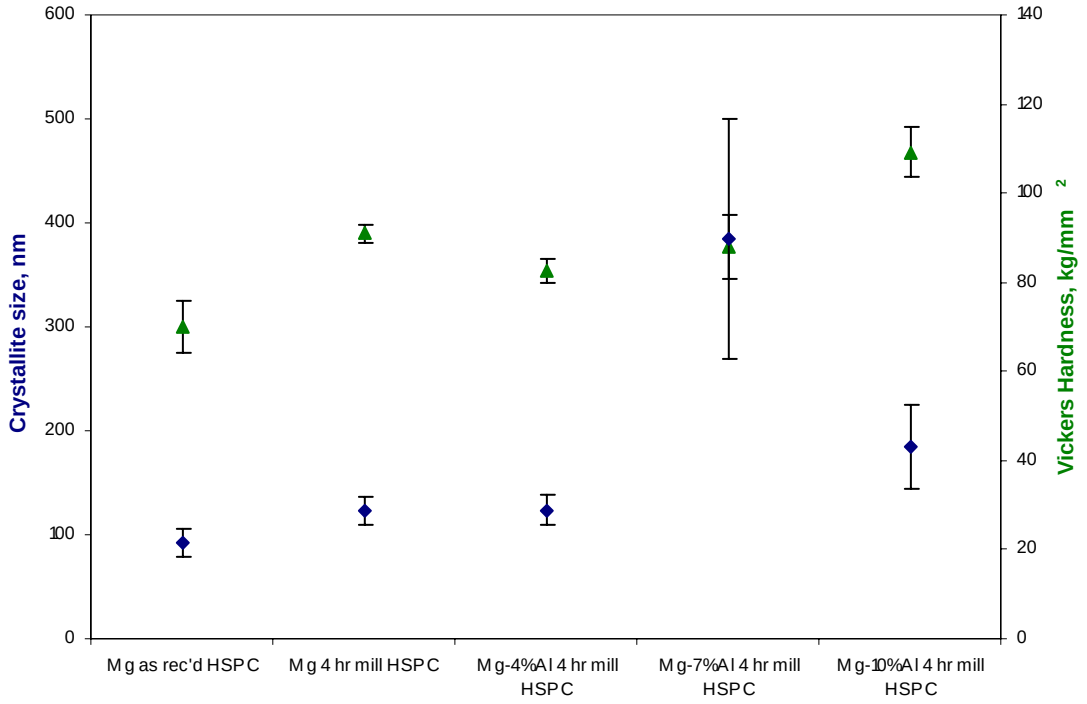

Figure 28: Crystallite size and Vickers hardness for consolidated Mg powders

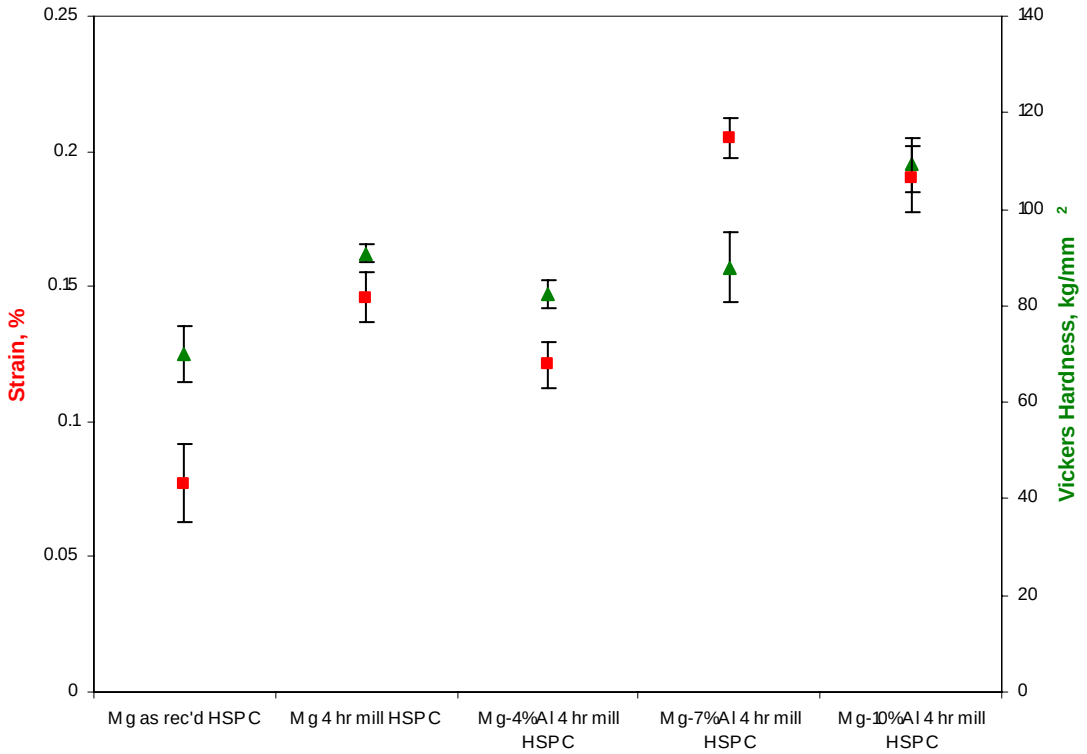

Figure 29: Strain and Vickers hardness for consolidated Mg powders

4.4.2.3 Fleischer Model for Solid Solution Strengthening

Figure 26 shows a relatively significant increase in hardness with the addition of Mg solute to Al solvent. Conversely, Figure 28 shows that when Al solute is added to Mg solvent, the hardness increase is much less. This apparent asymmetry in response may be a consequence of mechanistic influences known to be influential in solid solution strengthening, and may be illustrated through the application of the Fleischer predictive model [25].

Solid solution strengthening occurs as a consequence of an interaction between the strain fields associated with misfitting solute atoms and dislocations. Dislocations will tend to be either attracted (anchored) or repelled by misfitting solute depending upon the sense of the strain field generated by the solute and its position relative to the slip plane. Further, the self-energy of a dislocation will be influenced by the relative magnitude shear moduli between solute and solvent. In the latter regard, a "softer" solute (i.e., a solute of lower shear modulus) will serve to decrease the self-energy of a dislocation and will attract ("anchor") dislocations; a "harder" solute (i.e., higher modulus) will serve to repel dislocations. Fleischer devised a predictive model that serves to capture both effects for spherically-symmetric strain fields (i.e., substitutional solid solutions).

The magnitude of the size effect is initially quantified through the definition of the size interaction parameter, ε_b:

$$\varepsilon_b = \frac{1}{a_{solvent}} \cdot \frac{\Delta a}{\Delta c} \tag{8}$$

where $a_{solvent}$ is the lattice parameter of the solvent, and $\Delta a/\Delta c$ quantifies how the lattice parameter changes as solute is added. For an initial approximation, $\Delta a/\Delta c$ can be treated

as the Vegard's law approximation [7], which suggests that lattice parameters of solid solutions approximate a linear average between the values of the pure terminal elements or compounds.

The effect of modulus on the self-energy of a dislocation is similarly quantified through the modulus interaction parameter, ε_G:

$$\varepsilon_G = \frac{1}{G_{solvent}} \cdot \frac{\Delta G}{\Delta c} \tag{9}$$

where $G_{solvent}$ is the shear modulus of the solvent and $\Delta G/\Delta c$ provides an estimate of the sensitivity of modulus to solute additions. For purposes of approximation, $\Delta G/\Delta c$ for an alloy can likewise be estimated as a linear average between values of terminal elements or compounds.

Since the interaction of a screw dislocation with solute will be different than that for edge dislocations, Fleischer introduces a modified solute interaction parameter ε_G' which serves to average, or moderate, the effect of modulus differences:

$$\varepsilon_G' = \frac{\varepsilon_G}{1 + 0.5 \cdot |\varepsilon_G|} \tag{10}$$

The combined effects are quantified through a solid solution strengthening parameter, ε_{ss}:

$$\varepsilon_{ss} = \left| \varepsilon_G' - \beta \cdot |\varepsilon_b| \right| \tag{11}$$

where β is a constant of value approximately 3 for cubic metals.

Finally, a predictive value for the magnitude of solid solution strengthening ($\Delta\sigma_{sss}$) can be obtained through an equation that incorporates dislocation line energy and an estimation of the average solute (obstacle) spacing:

$$\Delta\sigma_{sss} \approx 2.8\times10^{-3}\cdot G\cdot\varepsilon_{ss}^{3/2}\cdot\sqrt{c} \qquad (12)$$

where c is the concentration of the solute in the alloy expressed as an atomic fraction.

Equations 11 and 12 predict that the size interactions are independent of the sign (i.e., independent of whether or not the solute is larger or smaller than the solvent), but that the sign of the modulus interaction will be influential. In particular, when ε_G' is negative, both the size and modulus effects additively contribute; when ε_G' is positive, the effects will partially cancel.

Table 4 lists the computed values for each of the above defined parameters.

Table 4: Computed values for Fleisher model parameters

	ε_b	ε_G	ε_G'	ε_{ss}
Al-x wt.% Mg	-0.205	-0.346	-0.295	0.910
Mg-x wt.% Al	+0.258	+0.529	+0.419	0.355

The predicted magnitudes for $\Delta\sigma_{sss}$ are plotted along with the measured change in hardness for the Al alloys in Figure 30 and the Mg alloys in Figure 31. The dashed line shows the predicted strengthening from the Fleischer model, and the data points indicate the hardness change from the as-received state.

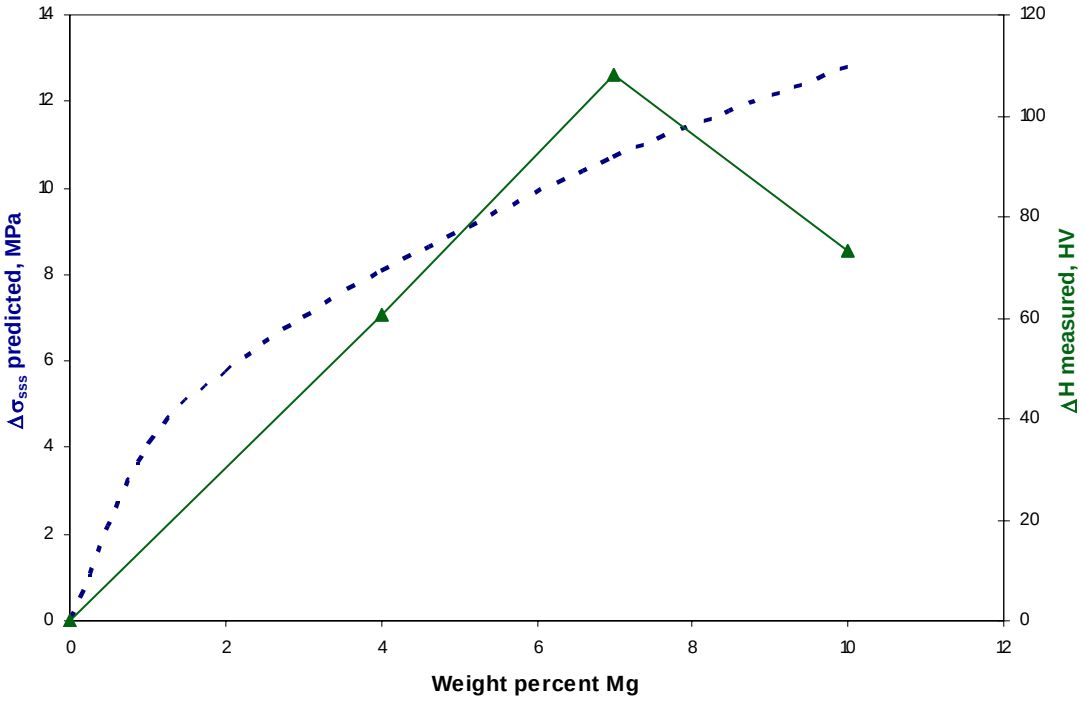

Figure 30: Predicted solid solution strengthening and measured hardness change in Al alloys

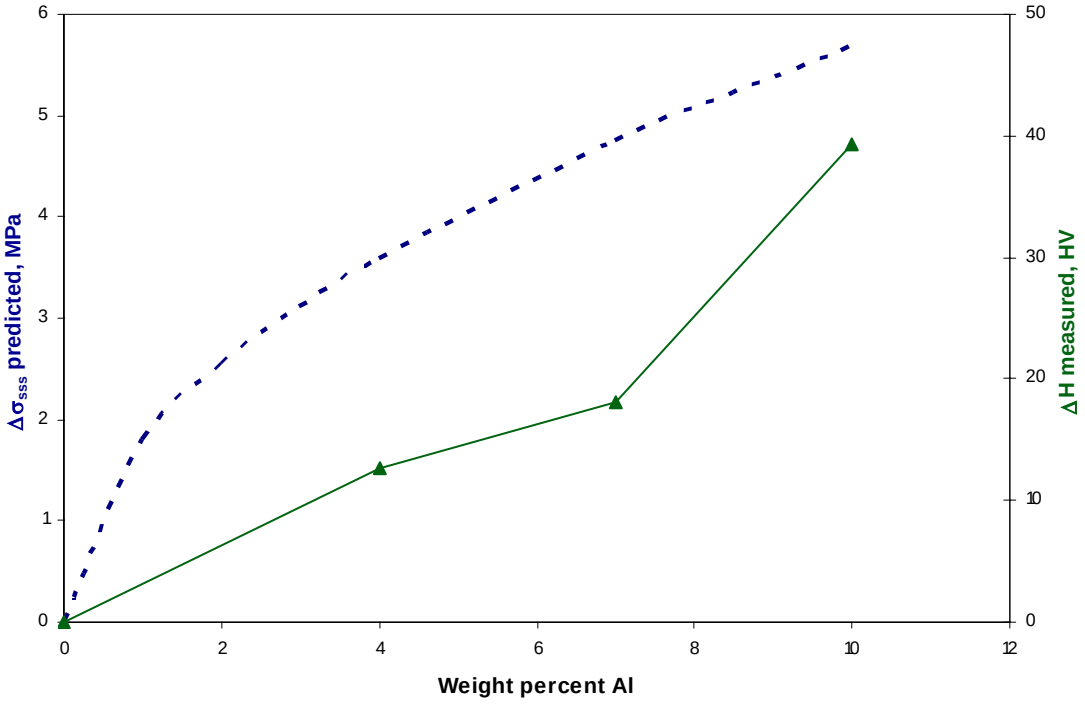

Figure 31: Predicted solid solution strengthening and measured hardness change in Mg alloys

The Fleischer model predicts the strengthening in both types of alloys reasonably well. The predicted magnitudes of solid solution strengthening are higher in Al alloys by a factor of 2.25, and the measured changes in hardness are higher by a factor of approximately 2 – 6.

4.4.2.4 Strengthening from Crystallite Refinement

The strengthening of a material by crystallite refinement was discussed in Chapters Two and Three. The Hall-Petch equation is used to quantify this effect, and is given as

$$\sigma_{ys} = \sigma_o + k_y \cdot d^{-1/2} \tag{1}$$

Figure 26 shows a significant decrease in grain size with the addition of Mg solute to Al solvent in the samples cryomilled for 4 hours. The Al as-received HSPC sample was found to have a crystallite size of 223.7 nm, while the 4, 7, and 10 wt.% Mg consolidated samples had sizes of 220.2, 51.4, and 76.1 nm, respectively. Based on this reduction, a positive change in strength ($\Delta\sigma_{gs}$) is expected for these alloys. Alternatively, when Al solute is added to Mg solvent, there is very little change in crystallite size. Figure 28 shows a crystallite size of 91.4 nm for the Mg as-received HSPC sample, and 124.0, 385.1, and 184.5 nm sizes for the alloyed samples. Thus, loss in strength is expected.

The predicted magnitudes for $\Delta\sigma_{gs}$ are plotted along with the measured change in hardness for the Al alloys in Figure 32 and the Mg alloys in Figure 33. The dashed line shows the predicted strengthening, and the data points indicate the hardness change from the as-received state. For elemental aluminum, the value of k is reported as 0.068 $MN/m^{3/2}$, and 0.279 $MN/m^{3/2}$ for magnesium [25].

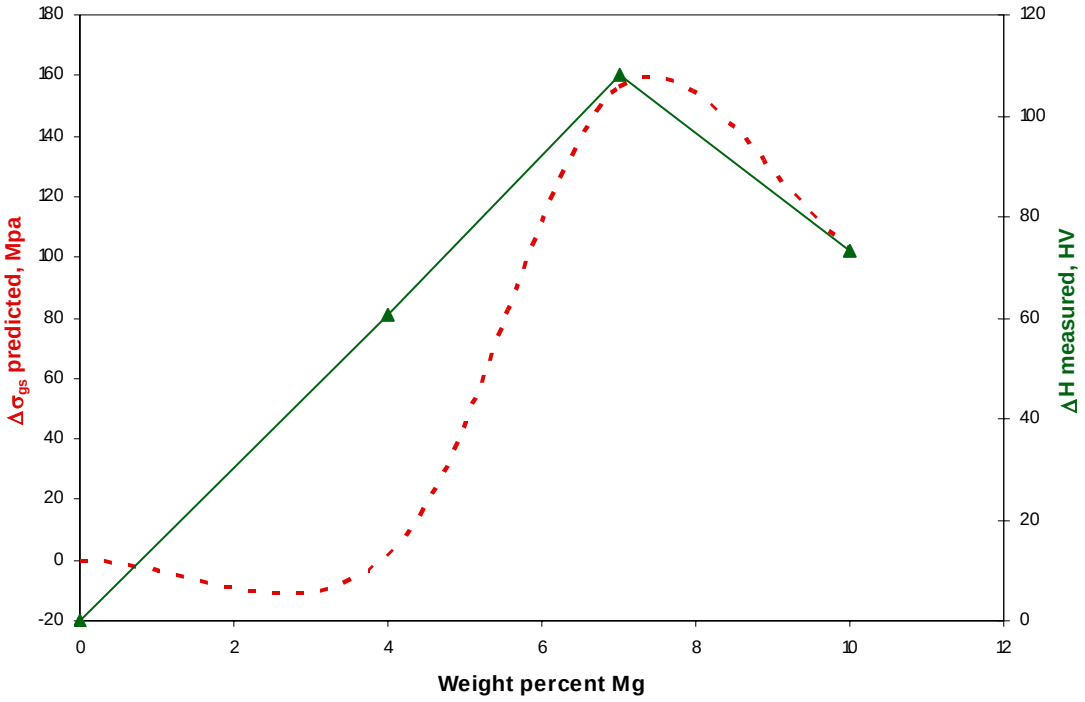

Figure 32: Predicted crystallite size strengthening and measured hardness change in Al alloys

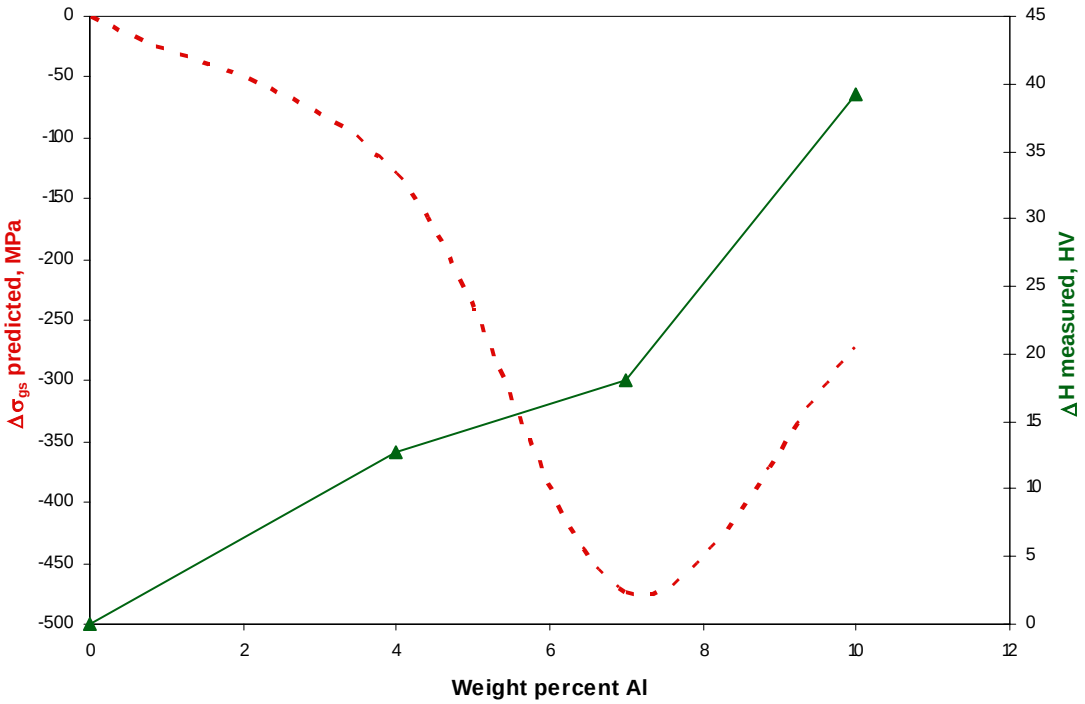

Figure 33: Predicted crystallite size strengthening and measured hardness change in Mg alloys

This relationship between predicted strengthening using the Hall-Petch equation and measured hardness is in correlation with similar experiments described in the literature [5]. The Hall-Petch equation predicts the strengthening in Al alloys exceptionally well. The predictions for Mg alloys, however, are unreasonable. The model does not predict strengthening due to crystallite size in Mg alloys for several reasons. The crystallites were larger than in the as-received state, which generates negative values for strengthening. Additionally, the reference stresses (σ_o) were assumed to be the same for all alloyed samples. The sensitivity of the Hall-Petch constant for Mg may also be to blame for these unreasonable values. The constant is fairly large for Mg, and when dealing with crystallite sizes in the nanometer range, the predicted magnitudes are prone to get out of proportion.

When these predictions are combined with those for solid solution strengthening, a summation of the two strengthening effects is considered. Because the Hall-Petch equation does not predict strengthening in Mg alloys well, this model's predictions were omitted from the Mg plot. The predicted magnitudes for $\Delta\sigma_{ys}$ are plotted along with the measured change in hardness for the Al alloys in Figure 34 and the Mg alloys in Figure 35. The dashed line shows the predicted strengthening, and the data points indicate the hardness change from the as-received state.

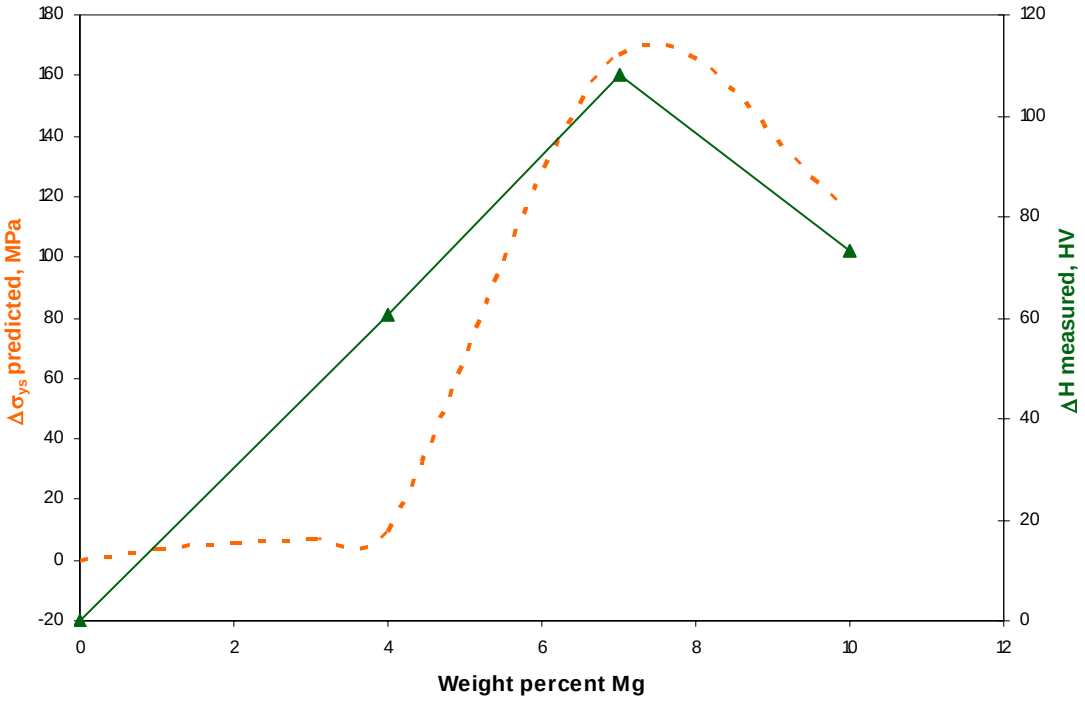

Figure 34: Predicted magnitude for combined strengthening and hardness change in Al alloys

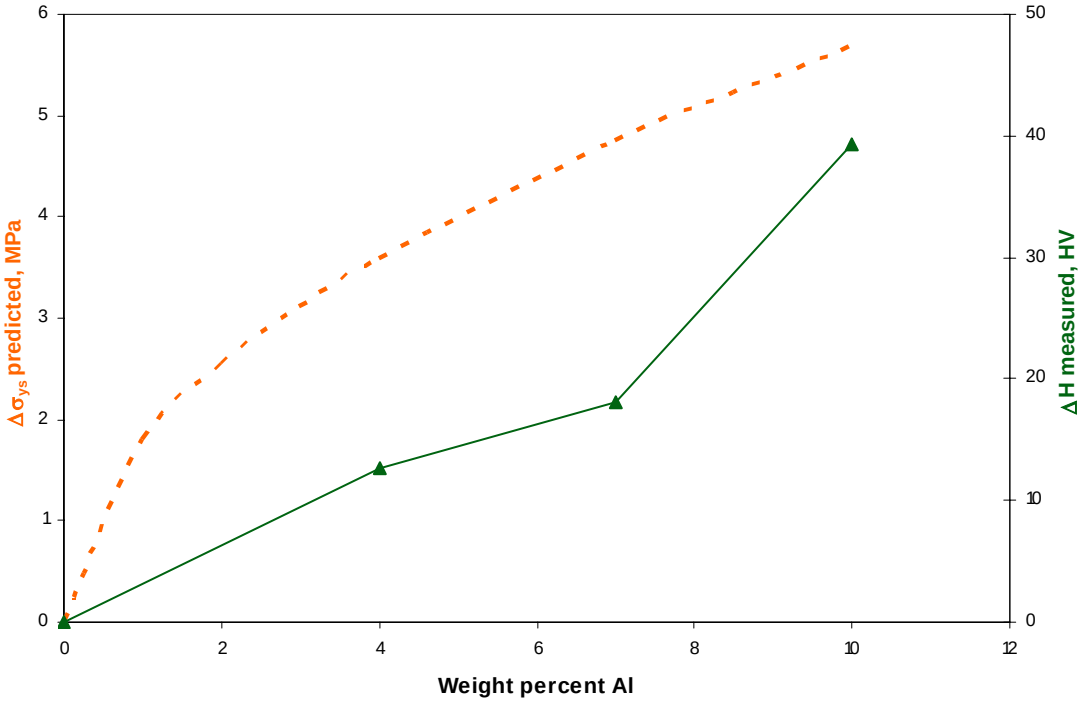

Figure 35: Predicted magnitude for combined strengthening and hardness change in Mg alloys

The predicted magnitudes for the combined strengthening effects of solid solution and crystallite refinement are very consistent with the measured change in hardness, at a factor of 2 – 3 for the Al alloys. The strengthening predicted for Mg alloys follows the trend in measured changes in hardness despite only the Fleischer model being used.

5 Chapter Five – Conclusions

This project was a preliminary study of cryomilling, including the conversion of an attritor ball mill to have cryogenic cooling capabilities. One major accomplishment in this area was the addition of a curved copper tube to direct the flow of liquid nitrogen as it enters the attritor can. By positioning this tube such that the flow of liquid nitrogen complements the rotation of the impeller and milling media, process yield was found to increase to over 90%. This not only reduces the loss of powder but also ensures that alloy composition remains essentially unchanged. This newly-adapted piece of equipment will be an asset in future experiments.

In general, the results indicate that cryomilling elemental powder decreases crystallite size in Al. Alternatively, there was no difference observed in Mg crystallite size after cryomilling. Cryomilling time did not significantly influence crystallite size in Al, however longer milling times did lead to a large increase in strain in the material. For both Al and Mg, the powder density was found to increase after cryomilling, suggesting the presence of small amounts of porosity in the as-received materials.

The addition of Mg to Al led to increases in crystallite size and strain, while it predictably lowered the measured density. Similarly, when Al was alloyed with Mg, crystallite size and strain increased. The density of these powders also increased as Al is denser than Mg.

The HSPC process proved to be a valuable tool to characterize the mechanical properties of nanocrystalline metal powders. Due to its low processing temperature, bulk nanocrystalline materials were formed without significant increases in crystallite size.

Dynamic recovery contributed to this crystallite size stability as well because HSPC provided mechanical deformation at the same time, unlike HIP.

Cryomilling increased the hardness of as-received Al by approximately 50% and as-received Mg by 30%. Alloying these two materials had even greater benefits in terms of strength. In Al, the addition of Mg more than doubled the hardness of the as-milled material. A Mg-10 wt.% Al sample had a hardness 56% greater than in its pure state.

The processing of metal powders by ball milling at cryogenic temperatures is a robust method of producing nanocrystalline materials. The sustained mechanical deformation at such low temperatures increases the material's stored energy, and thereby its strength. Strengthening is realized by crystallite size refinement and solid solution strengthening effects, in the case of an alloy. Models can predict the incremental strengthening effects to a reasonable measure. When the combined strengthening effects predicted by the Fleisher model and the Hall-Petch equation were considered, the predicted strength increase was consistent by a factor of 2 – 3 for Al alloys. The Hall-Petch equation was invalid for Mg alloys as crystallite size increased, and therefore predicted negative strengthening values. The Fleischer model predictions followed the trend in observed hardness change for Mg alloys.

6 Chapter Six – Future Work

Upon further study of the cryomilling process, there are several improvements that could be made. The current arrangement on the cryomill has one inlet line for liquid nitrogen to reach the attritor can. In order to cool down the can in an efficient manner, the pressure is initially adjusted to its maximum. However, once the powder sample is poured into the can, liquid nitrogen pressure of this magnitude will blow a portion of the powder up and out of the vent tubes. As this is quite undesirable, the pressure is lowered and carefully monitored while the temperature inside the can continues to cool down to -190°C. Two alterations to the set-up of the cryomill would benefit future projects. First, a second inlet line could be added and set at maximum pressure. This leaves the existing line for the lower pressure setting, allowing for a more consistent process, batch to batch. Secondly, the loss of powder is due, at least in part, to the build-up of head pressure by the evaporating liquid nitrogen. Larger diameter vent tubes, or simply more tubes, would alleviate this issue.

HSPC will be a useful technique as a low-temperature powder consolidation process. Studying the process variables will provide a greater understanding of its effect on the material, and generate more consistent results. Above all, the automation of the downward-applied pressure is critical to achieving repeatable results. A study of the effects of HSPC time and interface temperature on crystallite size would go a long way to understanding the process's capabilities.

In this study, x-ray diffraction was the only method used to quantify crystallite size. While x-ray diffraction yields good results, it does have its disadvantages. Ideally,

characterizing any material, especially nanocrystalline materials, should include more than one procedure [23]. Verification of the x-ray results could be achieved by transmission electron microscopy (TEM), including crystallite size distribution and shape [33]. Nearly all studies of cryomilled materials found in the literature use both x-ray diffraction and TEM. TEM of the materials in this experiment were not pursued due to time constraints and the unpredictable nature of sample preparation efforts. Not only would TEM confirm crystallite size, it could be used to characterize the concentration and location of the dispersed oxides and nitrides that are known to strengthen mechanically alloyed metal powders [34].

References

1. Park, Y.S., et al., *Microstructural investigation of nanocrystalline bulk Al-Mg alloy fabricated by cryomilling and extrusion.* Materials Science and Engineering A, 2004. **374**: p. 211-216.
2. Witkin, D., et al., *Al-Mg alloy engineered with bimodal grain size for high strength and increased ductility.* Scripta Materialia, 2003. **49**: p. 297-302.
3. Fecht, H.J., *Nanostructure formation by mechanical attrition.* Nanostructured Materials, 1995. **6**: p. 33-42.
4. Koch, C.C., *Synthesis of nanostructured materials by mechanical milling: Problems and opportunities.* Nanostructured Materials, 1997. **9**: p. 13-22.
5. Gubicza, J., et al., *The microstructure of mechanically alloyed Al-Mg determined by X-ray diffraction peak profile analysis.* Materials Science and Engineering A, 2004. **372**: p. 115-122.
6. Zhou, F., et al., *Formation of nanostructure in Al produced by a low-energy ball milling at cryogenic temperature.* Materials Science & Engineering A, 2004. **375-377**: p. 917-921.
7. Cullity, B.D. and S.R. Stock, *Elements of X-Ray Diffraction*. Third ed. 2001, Upper Saddle River, NJ: Prentice Hall.
8. Suryanarayana, C. and M.G. Norton, *X-Ray Diffraction: A Practical Approach*. 1998, New York: Plenum Press.
9. Hayes, R.W., V. Tellkamp, and E.J. Lavernia, *Creep behavior of a cryomilled ultrafine-grained Al-4%Mg alloy.* Journal of Materials Research, 2000. **15**(10): p. 2215-2222.
10. He, J., et al., *Quantitative analysis of grain size in bimodal powders by x-ray diffraction and transmission electron microscopy.* Journal of Materials Science, 2004. **39**: p. 6957-6964.
11. Lee, Z., et al., *Microstructure and microhardness of cryomilled bulk nanocrystalline Al-7.5%Mg alloy consolidated by high pressure torsion.* Scripta Materialia, 2004. **51**: p. 209-214.
12. Rodriguez, R., et al., *Tensile and creep behavior of cryomilled Inco 625.* Acta Materialia, 2003. **51**: p. 911-929.
13. Mohamed, F.A. and Y. Xun, *Correlations between the minimum grain size produced by milling and material parameters.* Materials Science and Engineering A, 2003. **354**: p. 133-139.
14. Zhou, F., K.H. Chung, and E.J. Lavernia, *Powder Metallurgy Alloys and Particulate Materials for Industrial Applications*, ed. A.E. Altman and J.W. Newkirk. 2000: Mineral, Metals, & Materials Society.
15. Zhang, D.L., T.B. Massalski, and M.R. Paruchuri, Metallurgical Material Transcripts A, 1994. **25**: p. 73.
16. Verhoeven, J., *Fundamentals of Physical Metallurgy*. 1975, New York: John Wiley & Sons.
17. Han, B.Q., E.J. Lavernia, and F.A. Mohamed, *Tension and compression behaviors of bulk ultrafine-grained Al-7.5 wt.% Mg alloy.* Philosophical Magazine Letters, 2003. **83**(2): p. 89-96.

18. Sevillano, J.G. and J. Aldazabal, *Ductilization of nanocrystalline materials for structural applications.* Scripta Materialia, 2004. **51**: p. 795-800.
19. Creehan, K. and J. Schultz, *Coating, Repair, and Modification of 2519 and 5083 Aluminum Using Friction Stir Fabrication*, in *N00014-05-1-0099*. 2005, Metalmorf Technologies, LLC: Christiansburg, VA.
20. Lloyd, D.J. *The Influence of Particles and Deformation Structure on Recrystallization*. in *Annual Meeting of TMS*. 1985. New York: The Metallurgical Society.
21. Morral, F.R., *Dispersion Strengthening of Metals*. 1977, Columbus, Ohio: Metals and Ceramics Information Center.
22. *Jade v. 6.5*. 2005, Materials Data Inc.: Livermore, CA.
23. Ungar, T., *The Meaning of Size Obtained from Broadened X-ray Diffraction Peaks.* Advanced Engineering Materials, 2003. **5**(5): p. 323-329.
24. Murray, J.L. *Aluminum-Magnesium Phase Diagram*. Metals Handbook Desk Edition [ASM Handbooks Online] 1988 [cited 2005; Second Edition:[Available from: http://products.asminternational.org/hbk/index.jsp.
25. Courtney, T.H., *Mechanical Behavior of Materials*. Second Edition ed. 2000, New York: McGraw-Hill.
26. Rodriguez-Carvajal, J., *Structural Analysis from Powder Diffraction Data: The Rietveld Method*. 1997, Ecole Thematique: Cristallographie et Neutrons: Gif sur Yvette Cedex, France. p. 1-25.
27. Shen, Y., H.H. Hng, and J.T. Oh, *Synthesis and characterization of high-energy ball milled Ni-15%Fe-5%Mo.* Journal of Alloys and Compounds, 2004. **379**: p. 266-271.
28. Oleszak, D. and P.H. Shingu, *Nanocrystalline metals prepared by low-energy ball milling.* Journal of Applied Physics, 1996. **79**(6): p. 2975-2980.
29. Callister, W.D., *Materials Science and Engineering: An Introduction*. Third ed. 1994, New York: John Wiley & Sons, Inc.
30. *Metals Handbook Desk Edition*. Third ed. ASM Handbooks. Vol. 2. 2002: ASM International.
31. Smith, W.F., *Structure and Properties of Engineering Alloys*. Second ed. 1993, New York: McGraw-Hill, Inc.
32. Zhang, X., et al., *Evidence for the formation mechanism of nanoscale microstructures in cryomilled Zn powder.* Acta Materialia, 2001. **49**: p. 1319-1326.
33. Jiang, H.G., M. Ruehle, and E.J. Lavernia, *On the applicability of the x-ray diffraction line profile analysis in extracting grain size and microstrain in nanocrystalline materials.* Journal of Materials Research, 1999. **14**(2): p. 549-559.
34. Karnthaler, H.P., et al., *TEM of nanostructured metals and alloys.* Materials Science and Engineering A, 2004. **387-389**: p. 777-782.

Appendix A: SEM Images of As-received Powder Samples

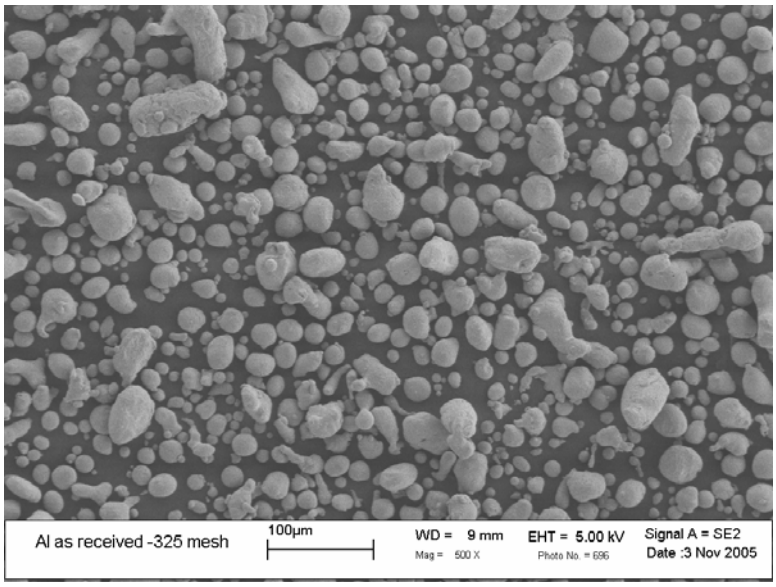

Figure 36: Scanning electron micrograph of as-received Al powder

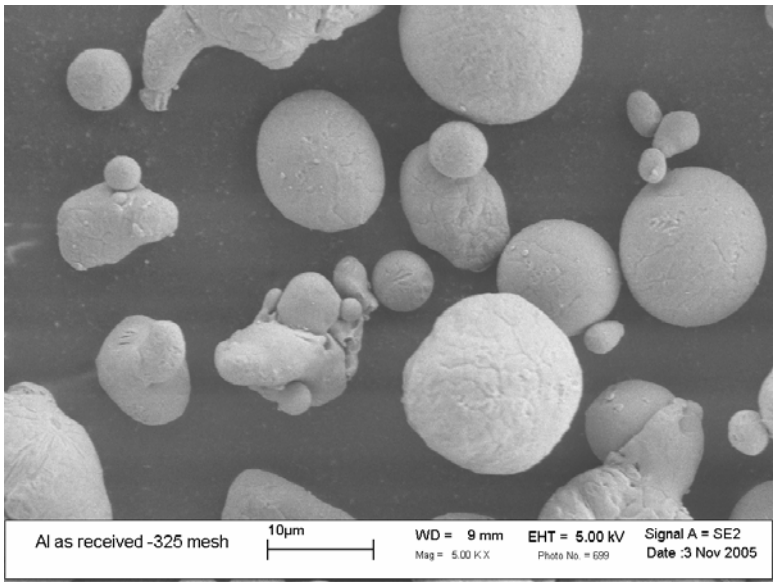

Figure 37: Scanning electron micrograph of as-received Al powder

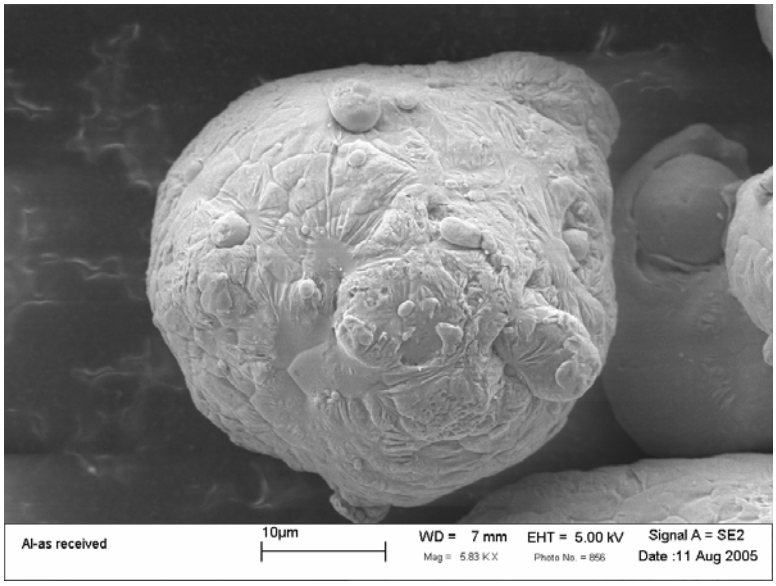

Figure 38: Scanning electron micrograph of as-received Al powder

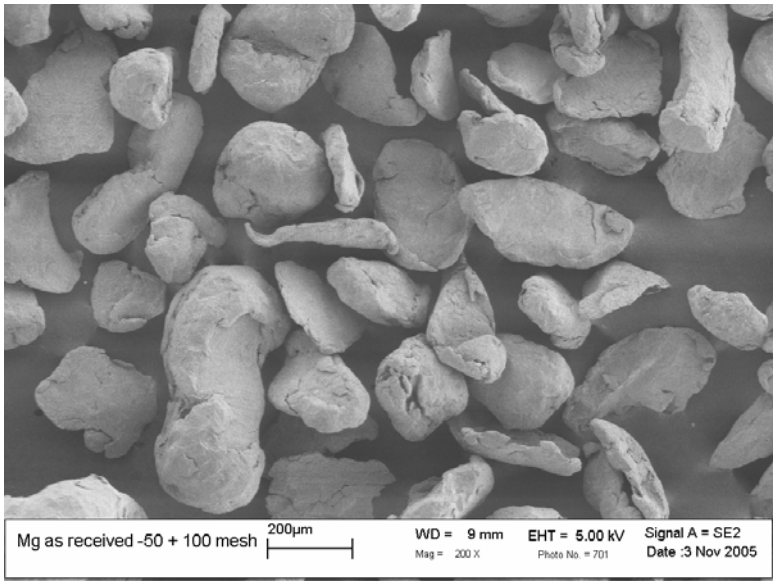

Figure 39: Scanning electron micrograph of as-received Mg powder

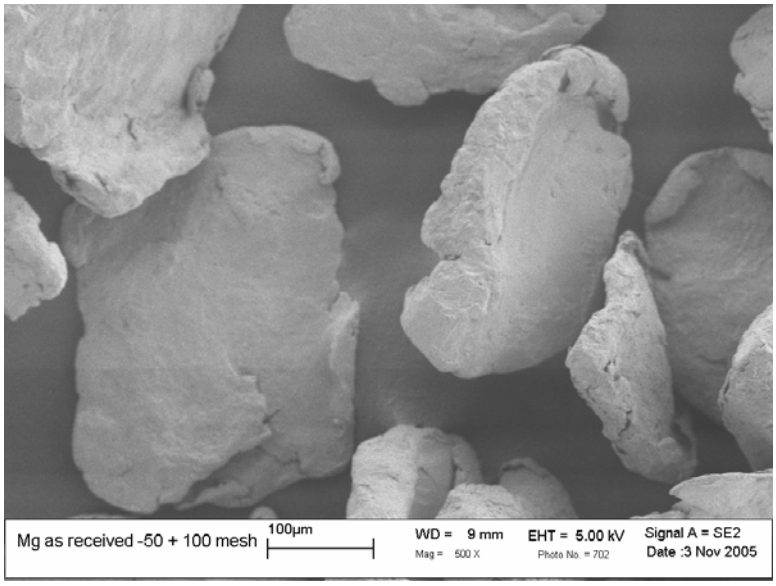

Figure 40: Scanning electron micrograph of as-received Mg powder

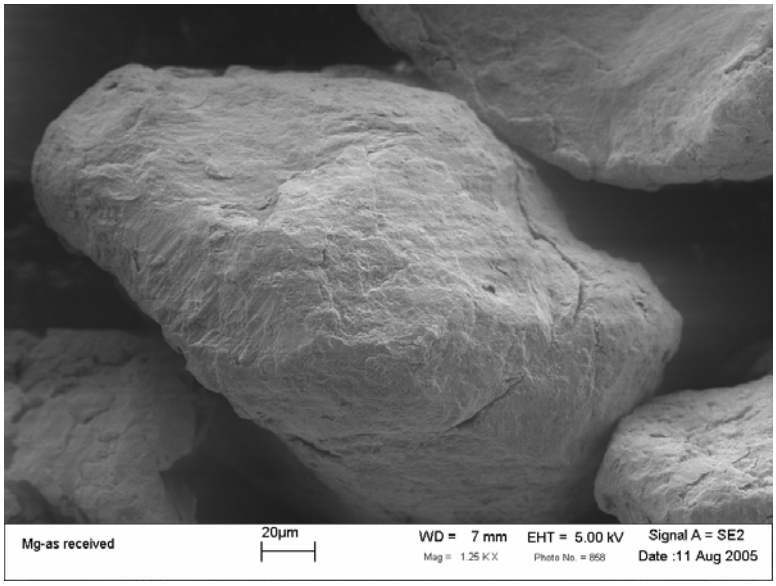

Figure 41: Scanning electron micrograph of as-received Mg powder

Appendix B: Derivation of Powder Density Equations

Table 5: List of terms for powder density equations

Symbol	Description
P_a	Ambient pressure
P_1	Elevated pressure
P_2	Intermediate pressure where $P_a < P_2 < P_1$
V_c	Volume of calibrated sample cell
V_s	Volume of sample
V_e	Volume of calibrated expansion cell
n_c	Number of moles of gas in sample cell
n_e	Number of moles of gas in expansion cell
R	Gas constant
T_a	Ambient temperature
m_s	Mass of sample
ρ_s	Density of sample

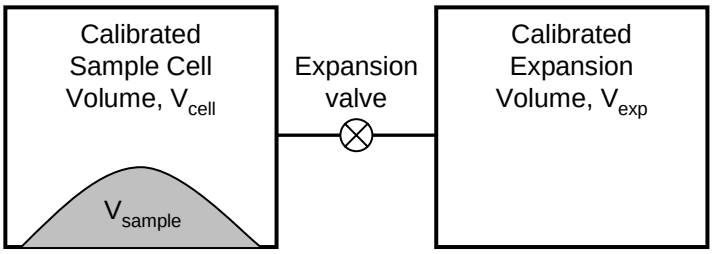

Figure 42: Simplified diagram of pycnometer chambers

Assume that both V_c and V_e are at ambient pressure and temperature. The valve is then closed and V_c is charged to an elevated pressure, P_1. The mass balance equation across the sample cell is

$$P_1 \cdot (V_c - V_s) = n_c \cdot R \cdot T_a \tag{13}$$

The mass equation for the expansion volume is

$$P_a \cdot V_e = n_e \cdot R \cdot T_a \tag{14}$$

When the valve is opened, the pressure will fall to an intermediate value, P_2, and the mass balance equation becomes

$$P_2 \cdot (V_c - V_s + V_e) = n_c \cdot R \cdot T_a + n_e \cdot R \cdot T_a \tag{15}$$

Substituting from equations (1) and (2) into (3) and simplifying gives

$$P_2 \cdot (V_c - V_s + V_e) = P_1 \cdot (V_c - V_s)_a + P_a \cdot V_e \tag{16}$$

$$(P_2 - P_1)(V_c - V_s) = (P_a - P_2) \cdot V_e \tag{17}$$

$$V_c - V_s = \frac{P_a - P_2}{P_2 - P} \cdot V_e \tag{18}$$

Adding and subtracting P_a in the denominator and rearranging gives

$$-V_s = -V_c + \frac{(P_a - P_2) \cdot V_e}{(P_2 - P_a) - (P_1 - P_a)} \tag{19}$$

Dividing by $(P_a - P_2)$ in both the numerator and denominator gives the volume of the sample as

$$V_s = V_c - \frac{V_e}{-1 - \dfrac{(P_1 - P_a)}{(P_a - P_2)}} \tag{20}$$

$$V_s = V_c - \frac{V_e}{\dfrac{(P_1 - P_a)}{(P_2 - P_a)} - 1} \tag{21}$$

The pycnometer uses this sample volume and the sample mass provided by the user to find density using

$$\rho_s = \frac{m_s}{V_s} \tag{22}$$

VITA

Adam grew up in Carlisle, Pennsylvania. During high school he studied in Soltau, Germany as a foreign exchange student. After graduating from Carlisle High School in 1999, Adam came to Virginia Tech where his athletic activities took a backseat to his engineering classes. He worked at Graham Packaging Company and NASA Langley during his undergraduate years and was a member of the Human-Powered Submarine Team of Virginia Tech for five years, serving as president in 2002-2003. In 2004, he set the world speed record for one-person, non-propeller driven submarine piloting *Specter*. Adam graduated from the MSE department in 2004 and stayed on for a master's degree in the department. Adam has begun working at Dominion Metallurgical in Roanoke, Virginia while finishing his degree.